

# Wafer-scale integration of graphene-based photonic devices

M. A. Giambra<sup>1,\*</sup>, V. Mišeikis<sup>2,3,\*</sup>, S. Pezzini<sup>2,3,4</sup>, S. Marconi<sup>5</sup>, A. Montanaro<sup>1</sup>, F. Fabbri<sup>2,3,4</sup>, V. Sorianello<sup>1</sup>, A. C. Ferrari<sup>6</sup>, C. Coletti<sup>2,3,#, §</sup> and M. Romagnoli<sup>1,#, §</sup>

<sup>1</sup>Photonic Networks and Technologies Lab, CNIT, Via G. Moruzzi 1, 56124 Pisa (Italy)

<sup>2</sup>Center for Nanotechnology Innovation @NEST - Istituto Italiano di Tecnologia, Piazza San Silvestro 12, I-56127 Pisa (Italy)

<sup>3</sup>Graphene Labs, Istituto Italiano di Tecnologia, Via Morego 30, 16163 Genova (Italy)

<sup>4</sup>NEST, Scuola Normale Superiore and Istituto Nanoscienze-CNR, Piazza San Silvestro 12, I-56127 Pisa, Italy

<sup>5</sup>Photonic Networks and Technologies Lab, Tecip Institute, Scuola Superiore Sant'Anna, Via G. Moruzzi 1, 56124 Pisa (Italy)

<sup>6</sup>Cambridge Graphene Centre, Cambridge University, 9 J.J. Thompson, Cambridge, UK.

\*These authors have contributed to this work equally

# [camilla.coletti@iit.it](mailto:camilla.coletti@iit.it); [mromagnoli@cnit.it](mailto:mromagnoli@cnit.it) §Joint last co authors

**Abstract.** Graphene and related materials can lead to disruptive advances in next generation photonics and optoelectronics. The challenge is to devise growth, transfer and fabrication protocols providing high ( $\geq 5,000 \text{ cm}^2 \text{ V}^{-1} \text{ s}^{-1}$ ) mobility devices with reliable performance at the wafer scale. Here, we present a flow for the integration of graphene in photonics circuits. This relies on chemical vapour deposition (CVD) of single layer graphene (SLG) matrices comprising up to  $\sim 12,000$  individual single crystals (SCs), grown to match the geometrical configuration of the devices in the photonic circuit. This is followed by a transfer approach which guarantees coverage over  $\sim 80\%$  of the device area, and integrity for up to 150 mm wafers, with room temperature mobility  $\sim 5,000 \text{ cm}^2 \text{ V}^{-1} \text{ s}^{-1}$ . We use this process flow to demonstrate double SLG electro-absorption modulators with modulation efficiency  $\sim 0.25, 0.45, 0.75, 1 \text{ dB V}^{-1}$  for device lengths  $\sim 30, 60, 90, 120 \mu\text{m}$ . The data rate is up to 20 Gbps. Encapsulation with single-layer hBN is used to protect SLG during plasma-enhanced CVD of  $\text{Si}_3\text{N}_4$ , ensuring reproducible device performance. Our full process flow (from growth to device fabrication) enables the commercial implementation of graphene-based photonic devices.

## Introduction.

Graphene is ideally suited for photonics and optoelectronics.<sup>1–4</sup> In particular, for optical<sup>5</sup> and data communications<sup>2,5,6</sup>, including virtual internet servers and data centres.<sup>2</sup> In 2020, the global IP data traffic, mostly cloud and data centres, was in the range of several zettabyte (ZB),<sup>7</sup> *i.e.*  $>10^{21}$  bytes exchanged in one year. The connection of an ever-increasing number of people and things to the Internet (Internet of things, IoT<sup>8</sup>) is pushing the requirements in terms of bandwidth (BW), defined as amount of data exchanged per unit time,<sup>9</sup> and the energy consumed by a device to exchange one bit of information.<sup>10</sup> By 2023,  $>27$  Bn devices are expected to be connected.<sup>7</sup> COVID-19 has forced people worldwide to stay at home, working and learning remotely as never before.<sup>11</sup> This resulted in

an increase by 20-100% of the fixed residential network<sup>11</sup> and 10 to 20% change in traffic levels on the mobile network,<sup>11</sup> thus a renewed demand of traffic for applications, such as teleconferencing, video streaming, and online games.<sup>12</sup> Photonic technologies play a key role to satisfy these requirements. Photonic devices for next generation telecom and datacom networks require  $>100 \text{ Gb s}^{-1}$  BW per single lane,<sup>13</sup> small footprint ( $< \text{mm}^2$ ),<sup>14</sup> low loss of optical power within the device due to optical coupling ( $<1 \text{ dB}$ )<sup>15</sup> and propagation loss ( $< 2 \text{ dB cm}^{-1}$ ),<sup>16</sup> insertion loss (IL), *i.e.* power loss due to insertion of a device,<sup>17</sup>  $<5 \text{ dB}$ ,<sup>18,19</sup> low energy cost  $<1 \text{ mW/GHz}$  or, equivalently,  $<1 \text{ pJ/bit}$ <sup>20,21</sup> and low cost of manufacturing ( $< \$10/\text{Gb s}^{-1}$  in 2020,<sup>2</sup> decreasing to  $< \$1/\text{Gb s}^{-1}$  by 2025).<sup>22</sup> For these reasons, research efforts are ongoing and include photonic devices based on alternative to the established silicon on insulator, SOI,<sup>23</sup> and InP technologies.<sup>24</sup> Silicon photonics (SiP) modulators for  $\geq 30 \text{ Gbaud}$  applications have IL  $\sim 2\text{--}3 \text{ dB}$  higher than InP- and LiNbO<sub>3</sub>-based modulators<sup>25</sup> because of the free carrier effect,<sup>26</sup> requiring device lengths in the mm scale. A baud is the symbol rate, whereby a symbol could convey more than one bit.<sup>27</sup> The bit rate is defined as baud rate times bits per symbol.<sup>17</sup> More compact and energy efficient devices were demonstrated exploiting resonant structures, *e.g.* microring resonators,<sup>28</sup> or the Franz-Keldish effect in Si-Ge alloys.<sup>29</sup> However, these devices have intrinsic wavelength selectivity.<sup>29</sup> InP technology provides modulators with size similar to SiP<sup>30</sup>, large BW ( $>50 \text{ GHz}$ ),<sup>31</sup> but with higher cost of manufacturing,<sup>31</sup> due to the greater cost of InP wafers with respect to Si ones.<sup>14,32,33</sup>

Graphene-based photonics is very promising, as graphene is fully compatible with SiP,<sup>2</sup> has electro-absorption,<sup>2,34</sup> electro-refraction,<sup>2,34</sup> and it can be used for light modulation<sup>2</sup> and photodetection.<sup>1,3</sup> The linear gapless energy-momentum relation of the massless Dirac Fermions in single layer graphene (SLG) leads to high mobility at room temperature RT ( $\mu > 100,000 \text{ cm}^2 \text{ V}^{-1} \text{ s}^{-1}$ )<sup>35–40</sup> and pronounced (more than 1 order of magnitude)<sup>35–38</sup> ambipolar electric field effect,<sup>41</sup> such that the surface conductivity,  $\sigma$ , can be tuned by applying a gate voltage.<sup>41</sup> The tuning of  $\sigma$  affects the optoelectronic properties of SLG.<sup>42,43</sup>  $\sigma$  is a complex quantity, affecting both absorption and refraction of light interacting with SLG.<sup>42</sup> When SLG is placed on a waveguide (WG) core, the guided light interacts with SLG, allowing a much larger absorption with respect to normal incidence.<sup>44</sup> The absorption coefficient for SLG on a SOI WG is up to  $0.1 \text{ dB } \mu\text{m}^{-1}$ ,<sup>45</sup> depending on SLG doping,<sup>45</sup> and distance from the WG core centre.<sup>46</sup> SLG has been used for electro absorption<sup>46,47</sup> and electro refraction modulation,<sup>48,49</sup> switching,<sup>50</sup> and photodetection.<sup>1-3,51–55</sup> Ref.<sup>46</sup> reported electro-absorption modulators (EAMs) based on SLG transferred on a  $7 \text{ nm Al}_2\text{O}_3$  layer deposited on a Si WG. This configuration was improved by using a SLG-insulator-SLG stack, *i.e.* a double SLG (DSLGS),<sup>2</sup> on an undoped Si WG.<sup>45,47,56</sup> This has two main advantages: 1) the use of a passive WG platform, *i.e.* pure dielectric WGs, without implantation or epitaxy processes typically employed in SiP<sup>57,58</sup> or InP,<sup>31</sup> simplifying the manufacturing process, with a consequent cost reduction; 2) enhanced modulation due to the interaction of two SLGs with the WG mode.<sup>34</sup> Single mode WGs have typical dimensions which depend on the refractive index of the guiding material.<sup>59</sup> SiP single mode WGs, guiding only

the fundamental mode,<sup>59</sup> have typical width  $\sim 480$  nm, when realized on 220 nm SOI.<sup>60</sup> Si<sub>3</sub>N<sub>4</sub> single mode WGs have larger width  $\sim 1$   $\mu\text{m}$ , depending on Si<sub>3</sub>N<sub>4</sub> thickness,<sup>39</sup> because of the lower refractive index ( $n=1.98$  for Si<sub>3</sub>N<sub>4</sub><sup>39</sup> compared to 3.47 for Si at 1550 nm).<sup>61</sup> The larger width of Si<sub>3</sub>N<sub>4</sub> WGs contributes to simplify the technology, because it requires less stringent lithography resolution, and also reduce costs, making small ( $\sim 10,000$  pieces/year) and medium ( $\sim 100,000$ - $1,000,000$  pieces/year) production volumes more affordable than in SOI or InP manufacturing lines.<sup>31</sup> This means that the volume (*i.e.* number of chips) threshold to implement a product in a Si fab can be reduced by using Si<sub>3</sub>N<sub>4</sub>. This enables the cost-effectiveness of medium-volume products ( $\sim 10,000$ - $100,000$  chips per year),<sup>2</sup> thus opening medium-volume (*e.g.*, long haul telecom optical systems) markets.<sup>2</sup>

To reach a high technology-readiness level (TRL  $>8$  *i.e.* System complete and qualified),<sup>62</sup> adequate for photonic device production, scalable techniques for SLG growth and transfer are needed. Chemical vapour deposition (CVD) on Cu yields SLG that, when encapsulated in hexagonal boron nitride (hBN), has electronic and structural quality (defect density, scattering time and  $\mu$ ) comparable to exfoliated SLG.<sup>35,37,38,63</sup> There has been significant progress for SLG scalable growth on dielectrics, such as SiO<sub>2</sub><sup>64</sup> and Al<sub>2</sub>O<sub>3</sub>,<sup>65</sup> and on CMOS-compatible Ge,<sup>66-68</sup> but with RT  $\mu$  limited to  $\sim 2000$  cm<sup>2</sup> V<sup>-1</sup> s<sup>-1</sup>.<sup>65</sup> Hence, as of 2020, the most common approach to obtain  $\mu > 5000$  cm<sup>2</sup> V<sup>-1</sup> s<sup>-1</sup> is to transfer SLG grown on Cu to the target substrate.<sup>69</sup> The so-called “wet” transfer<sup>70,71</sup> typically involves chemical etching Cu to release SLG.<sup>69,72</sup> Alternatively, SLG can be released from the growth substrate electrochemically<sup>73,74</sup> or by oxidizing Cu at the SLG interface.<sup>75</sup> The released SLG is then directly picked up from the aqueous solution using the target wafer, with alignment accuracy  $\geq 1$   $\mu\text{m}$ .<sup>76</sup> Wet-transferred SLG has  $\mu \sim 10^3$  cm<sup>2</sup> V<sup>-1</sup> s<sup>-1</sup>,<sup>69</sup> which can be improved by 2 orders of magnitude by hBN encapsulation.<sup>37</sup> “Fully dry” transfer<sup>35</sup> is based on direct pick-up of SLG from Cu using exfoliated flakes of hBN or other layered materials (LMs), such as WSe<sub>2</sub>.<sup>39</sup> In this approach, SLG is released from Cu and encapsulated without contact with water or solvents,<sup>35</sup> resulting in  $\mu > 3 \times 10^5$  cm<sup>2</sup> V<sup>-1</sup> s<sup>-1</sup> at RT.<sup>39</sup> Thus far, scalability is limited by the size of exfoliated hBN flakes (at present, up to  $\sim 100$   $\mu\text{m}$ ),<sup>77</sup> but CVD hBN or amorphous BN could be used in future to solve this. The “semi-dry” approach consists in SLG delamination from Cu in an aqueous solution either electrochemically<sup>76</sup> or by Cu oxidation,<sup>78</sup> followed by lamination on the target substrate in dry conditions. This yields  $\mu$  as high as in “fully dry” transfer after hBN encapsulation,<sup>38</sup> while allowing scalability.<sup>76</sup>

Here, we implement an aligned semi-dry transfer of SLG, based on electrochemical delamination in NaOH, and subsequent handling of a suspended polymer/SLG membrane using a frame. This approach avoids the contact of the target substrate with the aqueous solution, and enables deterministic placement of SLG single crystals (SC) with  $\sim 1$   $\mu\text{m}$  precision in X and Y in-plane, enabled by a transfer set-up equipped with micrometric actuators. We use a freestanding carrier membrane, comprising 2 polymer layers. This enables semi-dry transfer of large SLG matrices (up to  $\sim 12000$  SLG-SCs, limited to  $40 \times 40$  mm<sup>2</sup> by the dimensions of the CVD sample

enclosure)<sup>79</sup> with coverage >80% of the target photonics device area, and integrity in terms of SLG continuity, crucial for wafer-scale fabrication of photonic devices. We demonstrate wafer-scale fabrication of DSLG EAMs on Si<sub>3</sub>N<sub>4</sub> WGs based on a stack of two SLGs separated by ~17 nm Si<sub>3</sub>N<sub>4</sub>. We report 30 EAMs, on 4 chips from the same wafer, with uniform performance ±10%, demonstrating wafer-scale scalability and reproducibility of the complete process. We use monolayer (1L) CVD-hBN as a SLG encapsulation layer, to protect SLG during Si<sub>3</sub>N<sub>4</sub> deposition by plasma-enhanced CVD (PECVD). We get a contact resistance ~500 Ω μm for  $E_F > 0.2$  eV, allowing us to achieve a cut-off frequency, *i.e.* the frequency at which energy flowing through the system is reduced rather than passing through,<sup>17</sup> ~4 GHz for 120 μm EAMs, and ~12 GHz for 30 μm ones. The operation speed is ~20 Gb s<sup>-1</sup>, the highest data-rate achieved to date in Si<sub>3</sub>N<sub>4</sub> without using resonating devices. Higher speeds have only been demonstrated in Si<sub>3</sub>N<sub>4</sub> with resonating devices, *e.g.* SLG on Si<sub>3</sub>N<sub>4</sub> modulators working up to 22 Gb s<sup>-1</sup> were reported on microring resonators,<sup>56</sup> while up to 40 Gb s<sup>-1</sup> was demonstrated by using piezoelectric lead zirconate titanate (PZT) thin films on Si<sub>3</sub>N<sub>4</sub> microring resonators.<sup>80</sup> Due to the gapless nature of graphene,<sup>1-3,81</sup> graphene photonics can operate at any wavelength, unlike Refs.,<sup>56,80</sup> which were limited to the specific resonant wavelength.

## Results and Discussion

Our DSLG EAMs comprise two SLGs on a passive Si<sub>3</sub>N<sub>4</sub> WG, separated by a ~17 nm Si<sub>3</sub>N<sub>4</sub> dielectric, Fig. 1a. Three factors ensure scalable fabrication with reproducibility. (i) Wafer-scale source material with crystal size comparable to that of single devices, to avoid grain boundaries. (ii) Semi-dry transfer with low impact on SLG cleanliness and electrical properties. (iii) SLG protection prior and during dielectric deposition. In Ref. <sup>76</sup> we addressed (i), by preparing SLG SC matrices. This approach is compatible with the requirements of integrated photonics, allowing tailored growth of SLG according to the geometry of the photonic circuits. The lateral dimensions of the SLG SCs can be tuned from tens to hundreds μm.<sup>45,56,82</sup> The deterministic growth relies on pre-treating Cu by electropolishing, to reduce surface contaminations and improve surface flatness. Cu is then patterned with 5 μm Cr seeds at the desired SLG crystal locations. This is done by using optical lithography and thermal evaporation of 25 nm Cr. The growth is performed in a cold-wall CVD reactor (Aixtron BM Pro) at 1060 °C by using Ar annealing to maintain a low nucleation density (~10 crystals per mm<sup>2</sup>).<sup>79</sup> Due to residual oxidation in Cu, SLG nucleation requires surface impurities,<sup>83</sup> ensuring that SLG SCs nucleate only at the Cr seeds locations. The matrices of SLG SCs grown on Cu need to be released from the growth substrate and transferred to the target wafer (*e.g.*, a wafer containing WGs). To do so, we adapt our semi-dry transfer procedure,<sup>76</sup> and build a dedicated transfer tool. To facilitate handling, SLG is coated with a polymer carrier membrane and a semi-rigid Polydimethylsiloxane (PDMS) frame is attached to the Cu foil perimeter. The transfer itself consists of two stages: 1) wet SLG electrochemical delamination from the growth substrate and 2) dry SLG aligned lamination on the target substrate. After the SLG electrochemical release from Cu in NaOH

(see Methods for details), the SLG/polymer membrane is rinsed several times in deionised (DI) water and dried in air. The freestanding membrane is supported by the PDMS frame and can be handled in dry conditions. The SLG SCs are attached to the membrane holder of the lamination tool, which allows angle adjustment with  $\sim 0.1^\circ$  precision of the membrane with respect to the target wafer. The latter is brought in close proximity ( $\sim 500 \mu\text{m}$ ) to the membrane using a 4-axis micrometrical stage (X, Y, Z translation and  $\Theta$  rotation). After aligning the SLG-SCs to the photonic structures, the target wafer is heated to  $\sim 100^\circ\text{C}$  and brought into contact with SLG, resulting in adhesion with the target photonics chip over the whole membrane. The alignment is performed using a 12x zoom microscope lens attached to a Digital single-lens reflex (DSLR) camera. The PDMS frame is then detached from the sample, and placed in acetone for the polymer removal.

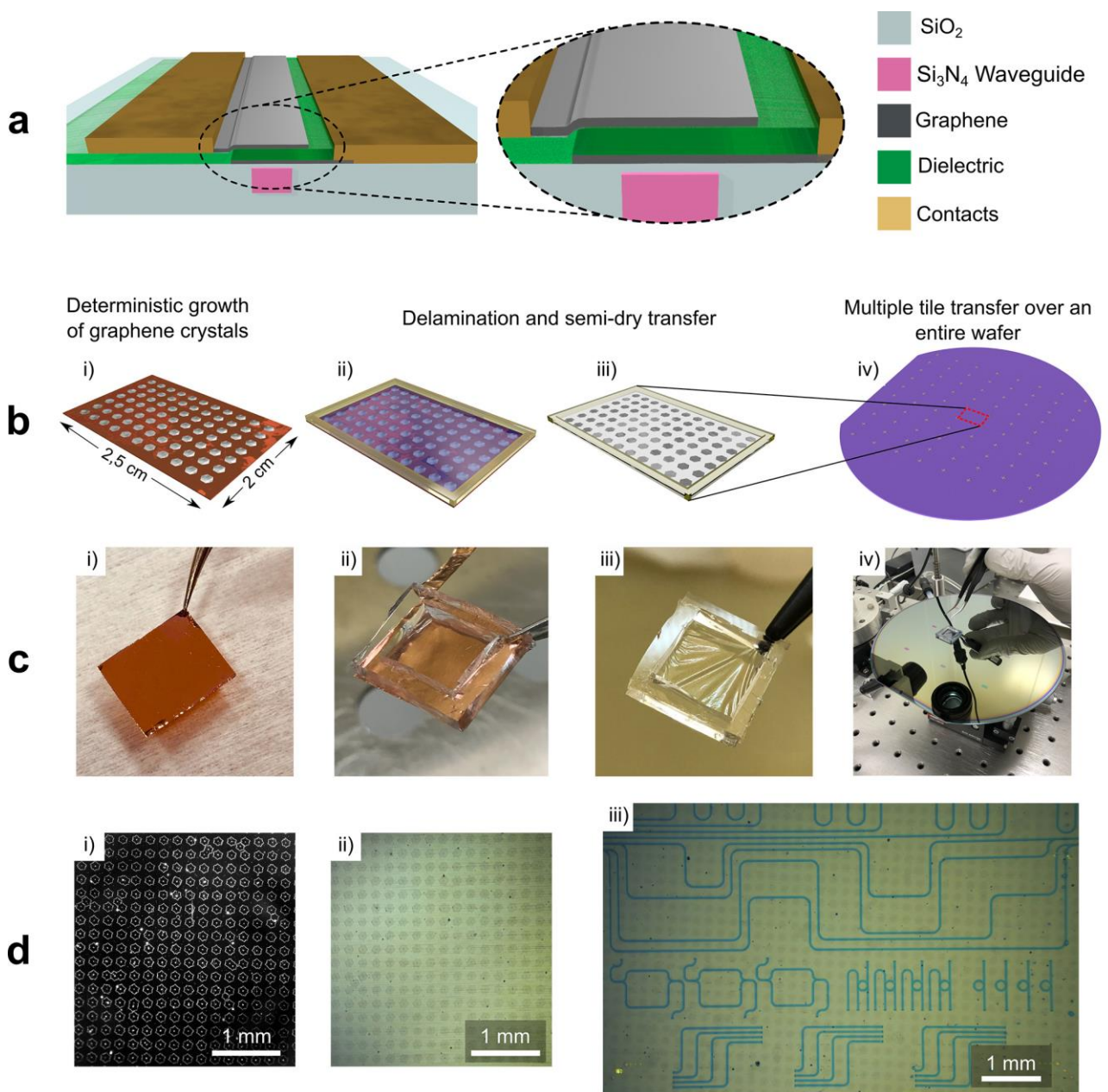


**Figure 1. Process flow. (a) Schematic cross-section of DSLG EAM. (b) Multiple tile stamping: i) schematic of SC-SLG matrix on Cu, ii) SC-SLG matrix on Cu covered with freestanding membrane and a frame, enabling aligned transfer, iii) delaminated SC-SLG matrix with freestanding membrane and frame, iv) transferred SLG on target wafer. (c) Photos of: i) as-grown SLG on Cu, ii) Cu with PDMS frame attached, iv) suspended polymer/SLG membrane and 150 mm photonic wafer with laminated SLG. (d) Optical micrographs of SC-SLG on Cu by dark field imaging, ii) suspended SLG-SCs on polymer membrane and iii) transferred SLG SC matrix on target wafer with photonic circuits.**

During the delamination of SLG from Cu and alignment to the target substrate, the freestanding polymer-SLG membrane is supported by a semi-rigid frame attached to the perimeter of the sample, Fig.1c. In Ref.,<sup>76</sup> the frame was made from polyimide (Kapton) tape and bonded to the sample using an adhesive, with the risk of chemical reaction with the NaOH electrolyte, thus contaminating the transferred SLG. To mitigate this, here we use PDMS-based support frames, which can be bonded to flat surfaces without any adhesive, thus ensuring transfer cleanliness. An alternative could be to use a solid Polydimethylsiloxane (PDMS) stamp,<sup>84</sup> which may also handle SLG. However, PDMS is not compatible with the lamination temperature (105 °C), due to its large ( $\sim 3.1 \times 10^{-4} \text{ K}^{-1}$ ) thermal expansion coefficient.<sup>85</sup> SLG-SCs attached to a PDMS stamps can develop nm-sized cracks when heated to 100 °C. Our method also relies on a bi-layer carrier polymer comprising 1.5  $\mu\text{m}$  poly(propylene carbonate) (PPC) and 100 nm PMMA, instead of the PMMA support of Ref.<sup>76</sup> The different glass transition temperatures,  $T_G$ , of PPC (37 °C)<sup>86</sup> and PMMA (105 °C)<sup>86</sup> allow us to have a membrane with variable mechanical properties, which can be controlled with T. At ambient T, during delamination and SLG SC alignment, both polymers are kept  $< T_G$ , thus providing a rigid support to the freestanding membrane and preventing SLG damage. When the SLG SCs are aligned to the required position on the target wafer, SLG can be laminated on the substrate by heating to  $\sim 100$  °C, well above the PPC  $T_G$ . The relatively thick and viscous PPC layer compared to PMMA allows the membrane to attach to the wafer and conform to surface structures, such as metal contacts, while retaining the integrity due to the solid, yet thin ( $\sim 100$  nm), PMMA layer, still below the PMMA  $T_G$ .<sup>87</sup> Crucially, in the lamination stage, the target substrate does not come into contact with an aqueous solution, therefore the transfer can be repeated on different areas of the same wafer without risk of SLG delamination or increased contamination. This enables the growth of SLG on a smaller scale, with greater control of strain and doping, than that currently achievable<sup>88,89</sup> when performing growth and transfer on full 150 or 200 mm wafers. The target wafer can then be populated *via* several transfers, as shown schematically in Fig.1b. Before each SLG transfer, photonics WGs are prepared by rinsing the chip in acetone and isopropanol, followed by a deep cleaning in a resist remover (AR-600 71) for 2 min. Following SLG transfer on the WGs, the fabrication of the DSLG stack is performed as follows. SLG is patterned and etched using electron-beam lithography (EBL) (Zeiss Ultra Plus) and reactive ion etching (RIE) (Sistec). The bottom SLG contacts are deposited *via* thermal evaporation of Ni/Au. A protective 1L-hBN film is transferred over the whole chip area using the semi-dry procedure described above. A 17 nm  $\text{Si}_3\text{N}_4$  gate dielectric is

deposited over the whole area.  $\text{Si}_3\text{N}_4$  is chosen over other dielectrics, such as  $\text{Al}_2\text{O}_3$ ,  $\text{HfO}_2$  or hBN, due its high breakdown field ( $>10 \text{ MV cm}^{-1}$ ).<sup>90</sup> PECVD can be used to deposit uniform  $\text{Si}_3\text{N}_4$  with thickness  $<20 \text{ nm}$  and Root Mean Square (RMS) roughness  $<0.5 \text{ nm}$ .<sup>90</sup> Top SLG SCs are then deposited using aligned semi-dry transfer. The top structure of the modulator is fabricated using identical methods to the bottom layer (see Methods for details). The SLG crystals are characterized throughout the fabrication process by Raman spectroscopy with a Renishaw InVia at  $532 \text{ nm}$ , laser power  $\sim 1 \text{ mW}$  and acquisition time  $\sim 4 \text{ s}$ . Fig.2b shows representative spectra of SLG on  $285 \text{ nm SiO}_2/\text{Si}$ , before (black) and after  $\text{Si}_3\text{N}_4$  deposition, with (orange) and without (dark cyan) capping of SLG with 1L-hBN (see sketch in Fig.2a). The Raman signature of 1L-hBN is extremely weak indicating the low quality of the commercial 1L-hBN.<sup>91</sup> The transferred SLG spectrum has a 2D peak with a single Lorentzian shape and with a full width at half-maximum  $\text{FWHM}(2\text{D}) \sim 26.7 \text{ cm}^{-1}$ , a signature of SLG.<sup>92</sup> The G peak position,  $\text{Pos}(\text{G})$ , is  $\sim 1583.7 \text{ cm}^{-1}$ , with  $\text{FWHM}(\text{G}) \sim 12.4 \text{ cm}^{-1}$ . The 2D peak position,  $\text{Pos}(2\text{D})$  is  $\sim 2676 \text{ cm}^{-1}$ , while the 2D to G peak intensity and area ratios,  $I(2\text{D})/I(\text{G})$  and  $A(2\text{D})/A(\text{G})$ , are  $\sim 3.1$  and  $\sim 6.8$ , respectively. No D peak is observed, indicating negligible defect concentration.<sup>93,94</sup> After  $\text{Si}_3\text{N}_4$  deposition, the Raman spectrum of exposed SLG (*i.e.* without 1L-hBN capping) has  $\text{Pos}(\text{G}) \sim 1590 \text{ cm}^{-1}$ ,  $\text{FWHM}(\text{G}) \sim 12 \text{ cm}^{-1}$ ,  $\text{Pos}(2\text{D}) \sim 2679 \text{ cm}^{-1}$ ,  $\text{FWHM}(2\text{D}) \sim 33.8 \text{ cm}^{-1}$ ,  $I(2\text{D})/I(\text{G}) \sim 1.8$ ,  $A(2\text{D})/A(\text{G}) \sim 5.1$ ,  $I(\text{D})/I(\text{G}) \sim 0.5$ . The latter indicates the creation of Raman active defects, which also act as scattering centres for the charge carriers<sup>95,96</sup> (one order of magnitude  $\mu$  decrease was reported in Ref.<sup>95</sup> when going from  $I(\text{D})/I(\text{G}) \sim 0.01$  to  $I(\text{D})/I(\text{G}) \sim 0.5$ ). Carrier scattering limits the performance of graphene EAMs, in terms of modulation efficiency (slope of the transmission variation as a function of applied voltage<sup>17</sup>) and maximum extinction ratio (ER),<sup>17</sup> (*i.e.* the ratio between maximum and minimum of light transmission<sup>17</sup>). The effect of defects on  $\text{FWHM}(\text{G})$ ,<sup>94</sup> which remains almost unchanged after  $\text{Si}_3\text{N}_4$  deposition, is likely compensated by the increased doping.<sup>97</sup> The Raman data indicate that the Fermi level ( $E_F$ ) of SLG after transfer is  $\sim 140 \text{ meV}$  (hole doping).<sup>98,99</sup>  $E_F$  in the exposed SLG increases to  $\sim 210 \text{ meV}$ .<sup>98,99</sup>

The SLG spectra with hBN capping after  $\text{Si}_3\text{N}_4$  deposition have  $\text{Pos}(\text{G}) \sim 1590 \text{ cm}^{-1}$ ,  $\text{FWHM}(\text{G}) \sim 11.8 \text{ cm}^{-1}$ ,  $\text{Pos}(2\text{D}) \sim 2684 \text{ cm}^{-1}$ ,  $\text{FWHM}(2\text{D}) \sim 32.5 \text{ cm}^{-1}$ ,  $I(2\text{D})/I(\text{G}) \sim 2.3$ ,  $A(2\text{D})/A(\text{G}) \sim 6.5$ . Fig.2c is a statistical comparison of  $I(\text{D})/I(\text{G})$  in 800 spectra from 2 SLG SCs with  $\text{Si}_3\text{N}_4$  on top (400 spectra each), one protected by 1L-hBN (orange), the other exposed to PECVD (dark cyan). 98% of the spectra on hBN-encapsulated SLG have  $I(\text{D})/I(\text{G}) < 0.1$ . 100% of the non-encapsulated SLG have  $I(\text{D})/I(\text{G}) > 0.1$ , with an average  $I(\text{D})/I(\text{G}) \sim 0.48$ , corresponding to a defect concentration  $\sim 1.4 \times 10^{11} \text{ cm}^{-2}$  (taking into account the finite doping ( $\sim 210 \text{ meV}$ )).<sup>94,100</sup> Hence, capping with 1L-hBN limits the creation of Raman active defects, therefore contributing to preserve  $\mu$ .<sup>95,96</sup> SLG SCs exposed to  $\text{Si}_3\text{N}_4$  deposition present cracked areas with an average crack size  $\sim 10 \mu\text{m}$ , as for the optical microscopy image in Fig. 2c (right inset).



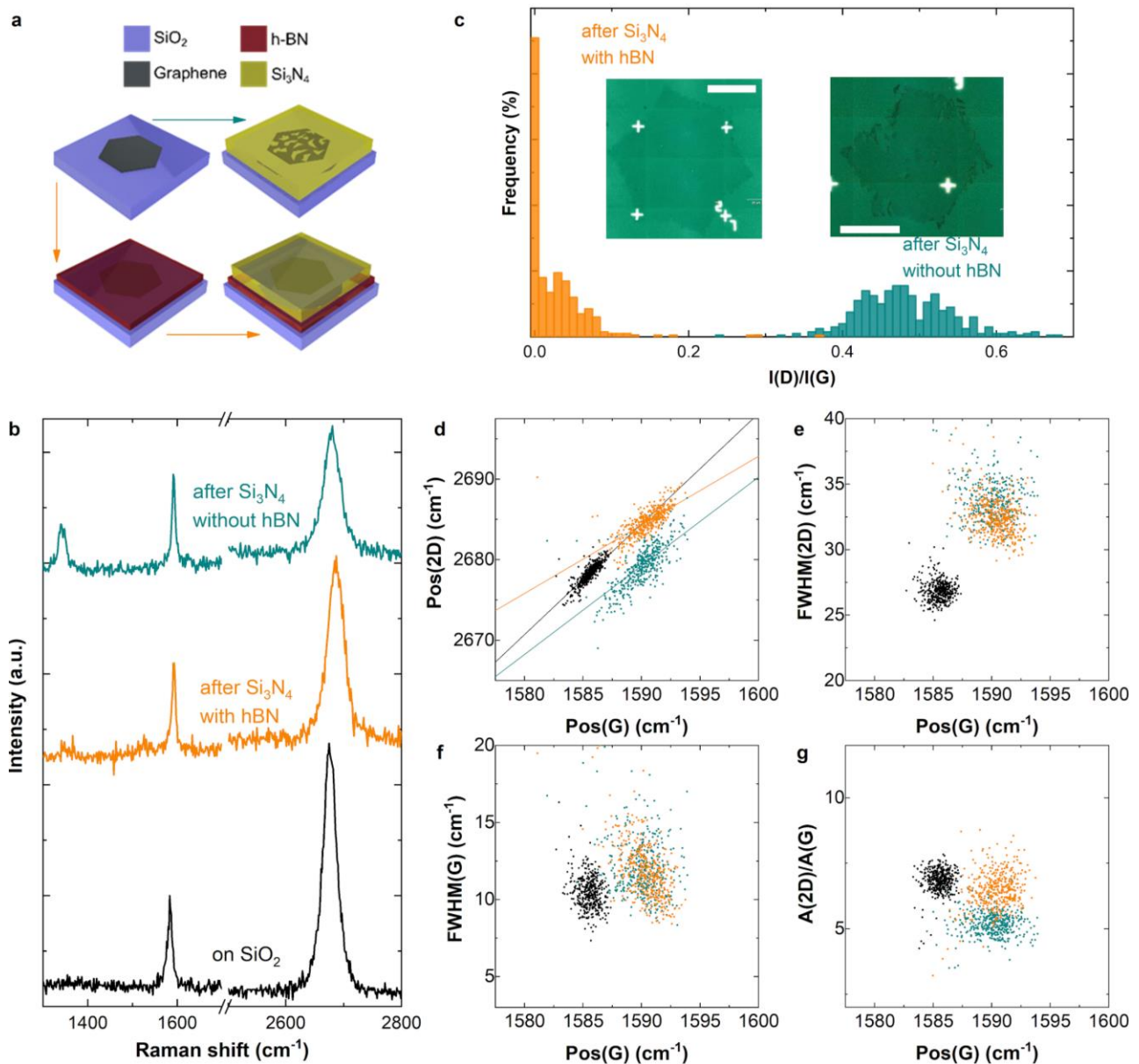


**Figure 2. Encapsulation of SLG thin film and protective 1L-hBN. (a) Schematic representation of PECVD deposition of Si<sub>3</sub>N<sub>4</sub> on SLG without (top, dark cyan arrow) and with (bottom, orange arrows) intermediate 1L-hBN. (b) Typical Raman spectra on SLG SCs after transfer (black) after Si<sub>3</sub>N<sub>4</sub> PECVD, with (orange) and without (dark cyan) 1L-hBN. The same colours are used in the correlation plots d-g. (c) Distribution of I(D)/I(G) from 800 spectra acquired on two SLG SCs, one protected (orange bars), the other exposed (dark cyan bars). Inset: optical micrographs of the two SCs, showing cracked areas in the exposed one. Scale bars 50  $\mu\text{m}$ . (d) Pos(2D) as a function of Pos(G). Solid lines are linear fits of the data. (e), FWHM(2D) as a function of Pos(G). (f) FWHM(G) as a function of Pos(G). (g) A(2D)/A(G) as a function of Pos(G).**

SLG capping with 1L-hBN it is also used to protect SLG during PECVD (at 350°C) of Si<sub>3</sub>N<sub>4</sub>. Raman mapping is performed at 1 $\mu\text{m}$  steps, over an area  $\sim 20 \mu\text{m} \times 20 \mu\text{m}$  on SLG transferred onto SiO<sub>2</sub>/Si, and after Si<sub>3</sub>N<sub>4</sub> deposition, with and without 1L-hBN. Figs.2d-g plot Raman data extracted



from the maps: Pos(2D), FWHM(2D), FWHM(G), A(2D)/A(G), as a function of Pos(G). Pos(G) depends on both doping<sup>98,99</sup> and strain.<sup>101</sup> This implies that local variations in strain and doping manifest as a spread in Pos(G), which in our SLG after transfer is  $1585.5 \pm 0.7 \text{ cm}^{-1}$ , and after Si<sub>3</sub>N<sub>4</sub> deposition with and without 1L-hBN is  $1590.3 \pm 1.5 \text{ cm}^{-1}$  and  $1590 \pm 1.6 \text{ cm}^{-1}$ , respectively. FWHM(2D) after transfer is  $\sim 26.9 \pm 0.8 \text{ cm}^{-1}$ , while an almost identical range of FWHM (2D) is measured after Si<sub>3</sub>N<sub>4</sub> deposition with and without hBN ( $\sim 32.5 \pm 1.5 \text{ cm}^{-1}$  and  $33.8 \pm 2 \text{ cm}^{-1}$ ). After transfer FWHM(G) is  $\sim 10.5 \pm 1 \text{ cm}^{-1}$ , Pos(2D) is  $\sim 2678 \pm 1.2 \text{ cm}^{-1}$ , I(2D)/I(G) and A(2D)/A(G) are  $\sim 2.6 \pm 0.3$  and  $\sim 6.8 \pm 0.6$ . After Si<sub>3</sub>N<sub>4</sub> deposition with hBN capping, FWHM(G)  $\sim 11.8 \pm 1.7 \text{ cm}^{-1}$ , Pos(2D)  $\sim 2684.6 \pm 1.8 \text{ cm}^{-1}$ , I(2D)/I(G) and A(2D)/A(G) are  $\sim 2.3 \pm 0.3$  and  $\sim 6.5 \pm 0.7$ , respectively. After Si<sub>3</sub>N<sub>4</sub> deposition without hBN capping, FWHM(G)  $\sim 12.0 \pm 1.9 \text{ cm}^{-1}$ , Pos(2D)  $\sim 2679.3 \pm 1.8 \text{ cm}^{-1}$ , I(2D)/I(G) and A(2D)/A(G) are  $\sim 1.8 \pm 0.2$  and  $\sim 5.1 \pm 0.5$ , respectively. The Raman data indicate E<sub>F</sub> after transfer  $\sim 140 \text{ meV}$  (hole doping).<sup>98,99</sup> HBN capping, in addition to limiting the generation of Raman active defects, keeps E<sub>F</sub> close to that of transferred SLG ( $\sim 150 \text{ meV}$ ). E<sub>F</sub> in exposed SLG increases to  $\sim 210 \text{ meV}$ .<sup>98,99</sup> The Grüneisen parameters<sup>101</sup> rule the change of Pos(2D) and Pos(G) in response to strain. The G and 2D peaks do (do not) split for increasing uniaxial (biaxial) strain.<sup>93</sup> At low ( $\leq 0.5\%$ ) strain the splitting cannot be resolved.<sup>101,102</sup> Fig.3d plots the correlation between Pos(2D) and Pos(G). Linear fits in Fig.3d give a slope  $\Delta\text{Pos}(2D)/\Delta\text{Pos}(G) \sim 1.37, \sim 0.85, \sim 1.1$  for SLG after transfer, after Si<sub>3</sub>N<sub>4</sub> with hBN and without hBN, respectively. The slopes indicate that both doping and strain variations are present. We cannot exclude the presence (or coexistence) of biaxial strain. For uniaxial (biaxial) strain, Pos(G) shifts by  $\Delta\text{Pos}(G)/\Delta\epsilon \sim 23(60) \text{ cm}^{-1}/\%$ .<sup>101-103</sup> For intrinsic SLG (E<sub>F</sub> < 100 meV), the unstrained, undoped Pos(G) is  $\sim 1581.5 \text{ cm}^{-1}$ .<sup>92,104</sup> Taking into account the shift in Pos(G) due to finite doping (E<sub>F</sub>  $\sim 140, 150, 210 \text{ meV}$  for the 3 cases), we estimate a mean uniaxial(biaxial) strain  $\epsilon \sim 0.03\%(\sim 0.01\%)$  for the transferred SLG, and  $\sim 0.22\% (\sim 0.08\%)$  and  $\sim 0.09\% (\sim 0.04\%)$  for the hBN-capped and exposed SLG after Si<sub>3</sub>N<sub>4</sub> deposition, respectively.

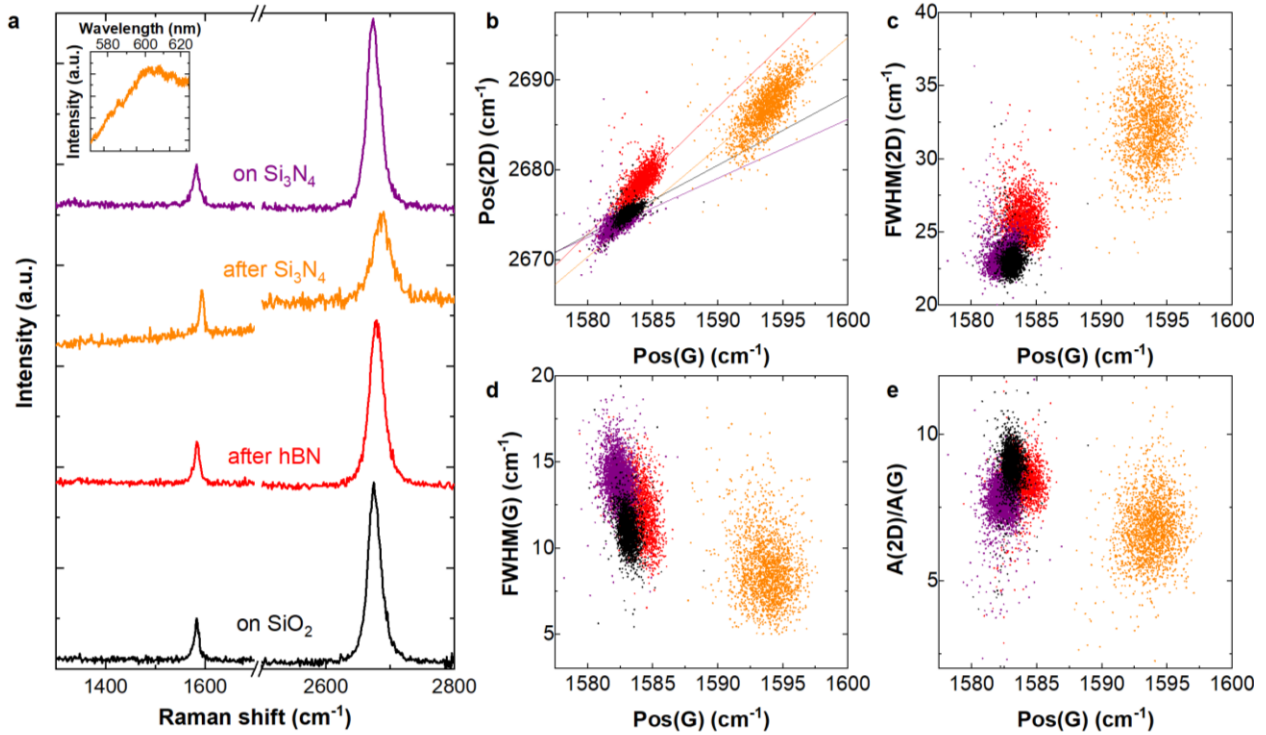


**Figure 3. Wafer-scale Raman measurements. (a) Representative spectra of SLG SCs for the different fabrication steps, Inset: photo-luminescence of 1L-hBN after  $\text{Si}_3\text{N}_4$  deposition. (b-e) Pos(2D), FWHM(2D), FWHM(G), A(2D)/A(G) as a function of Pos(G). The colour code is the same as in panel a.**

After 1L-hBN-capping and PECVD deposition of  $\text{Si}_3\text{N}_4$ , DSLGs are completed by transferring top-layer SLG arrays onto  $\text{Si}_3\text{N}_4$  by semi-dry transfer. The use of identical deterministically-grown SC matrices ensures that bottom and top SLG overlap over the entire wafer area, enabling wafer-scale fabrication. The assembly of DSLG is monitored by Raman spectroscopy. We collect 8909 spectra on 48 crystals (24 bottom-layer and 24 top-layer) over 4 portions of a 150 mm wafer (p-doped Si with 285nm  $\text{SiO}_2$ ). Fig.3a plots representative spectra taken after the main assembly steps: 1) transfer of bottom SLG arrays on  $\text{SiO}_2/\text{Si}$  (black), 2) transfer of 1L-hBN (red), 3) deposition of  $\text{Si}_3\text{N}_4$  (orange), and 4) transfer of top SLG on  $\text{Si}_3\text{N}_4$  (purple). The SLG spectra after transfer on  $\text{SiO}_2$  (bottom-layer, black) and on  $\text{Si}_3\text{N}_4$  (top-layer, purple) have a 2D peak with a single Lorentzian shape and with  $\text{FWHM}(2\text{D}) \sim 22.2$  and  $\sim 23.1 \text{ cm}^{-1}$ , respectively. Pos(G), is  $\sim 1583.1 \text{ cm}^{-1}$  for SLG on  $\text{SiO}_2$  and  $\sim 1582.1 \text{ cm}^{-1}$  for SLG on  $\text{Si}_3\text{N}_4$ , with  $\text{FWHM}(\text{G}) \sim 10.6$  and  $\sim 14.5 \text{ cm}^{-1}$ , respectively. Pos(2D) is  $\sim 2675.3$  and  $\sim 2673.9 \text{ cm}^{-1}$ , while  $I(2\text{D})/I(\text{G})$  and  $A(2\text{D})/A(\text{G})$ , are  $\sim 4.5$  (on  $\text{SiO}_2$ ),  $\sim 5$  (on  $\text{Si}_3\text{N}_4$ ), and  $\sim 9.5$  (on  $\text{SiO}_2$ ),  $\sim 8$  (on  $\text{Si}_3\text{N}_4$ ). No D peak is observed, indicating negligible defect concentration.<sup>93,94</sup> The difference in  $\text{FWHM}(\text{G})$  indicates reduced doping for the top-layer SLG on  $\text{Si}_3\text{N}_4$ .<sup>98,105</sup> The bottom-layer SLG spectra with hBN capping before (red) and after (orange)  $\text{Si}_3\text{N}_4$  deposition have both a 2D peak with a single Lorentzian shape and  $\text{FWHM}(2\text{D}) \sim 24.6$  and  $\sim 32.2 \text{ cm}^{-1}$ . Pos(G) is  $\sim 1583.9$  and  $\sim 1593.6 \text{ cm}^{-1}$  for hBN-capped SLG before and after  $\text{Si}_3\text{N}_4$  deposition, with  $\text{FWHM}(\text{G}) \sim 11.4$  and  $\sim 8.6 \text{ cm}^{-1}$ , Pos(2D)  $\sim 2678.7$  and  $\sim 2686.8 \text{ cm}^{-1}$ .  $I(2\text{D})/I(\text{G})$  and  $A(2\text{D})/A(\text{G})$  are  $\sim 4.1$  and

~8.9 before, and ~1.9 and ~7.2 after the Si<sub>3</sub>N<sub>4</sub> deposition. The shift of Pos(G) and decrease of FWHM(G), together with decrease of I(2D)/I(G) and A(2D)/A(G), indicate an increase in E<sub>F</sub> upon Si<sub>3</sub>N<sub>4</sub> deposition.<sup>98,99</sup> In addition, a considerable (2500 cps at 1 mW power excitation) photoluminescence background is observed after Si<sub>3</sub>N<sub>4</sub> deposition, which we attribute to the introduction of defects in 1L-hBN.<sup>106</sup> The broad band is peaked at 600 nm (inset, Fig.3a) similar to defect related broad emission in 1L-hBN.<sup>106</sup> Raman mapping is then performed on the SLG arrays at 10µm steps. Figs.3b-e plot Pos(2D), FWHM(2D), FWHM(G), A(2D)/A(G), as a function of Pos(G). Local variations in strain<sup>98</sup> and doping<sup>98,99</sup> produce a spread in Pos(G), which in bottom-layer SLG after transfer, after 1L-hBN capping, after Si<sub>3</sub>N<sub>4</sub> deposition, and in the top-layer SLG is 1583.1 ± 0.5, 1584 ± 0.9, 1593.8 ± 1.4 and 1582.3 ± 0.7 cm<sup>-1</sup>, respectively. FWHM(2D) increases after each fabrication step on bottom-layer SLG, from ~23 ± 0.8 cm<sup>-1</sup> after transfer, to 25.9 ± 1.3 cm<sup>-1</sup> after 1L-hBN capping, and 32.7 ± 2.6 cm<sup>-1</sup> after Si<sub>3</sub>N<sub>4</sub> deposition. For the top-layer SLG, FWHM(2D) is ~23.4 ± 1 cm<sup>-1</sup>, similar to the transferred bottom-layer. After transfer, FWHM(G) is ~11 ± 1.1 cm<sup>-1</sup>, Pos(2D) is ~2675.2 ± 0.6 cm<sup>-1</sup>, I(2D)/I(G) and A(2D)/A(G) are ~4.3 ± 0.4 and ~8.9 ± 0.7. After hBN capping, FWHM(G) ~12.2 ± 1.5 cm<sup>-1</sup>, Pos(2D) ~2678.5 ± 1.7 cm<sup>-1</sup>, I(2D)/I(G) and A(2D)/A(G) are ~3.9 ± 0.4 and ~8.4 ± 0.8, respectively. After Si<sub>3</sub>N<sub>4</sub> deposition, FWHM(G) ~8.8 ± 1.9 cm<sup>-1</sup>, Pos(2D) ~2687.1 ± 2.6 cm<sup>-1</sup>, I(2D)/I(G) and A(2D)/A(G) are ~1.8 ± 0.3 and ~6.8 ± 1.1, respectively. In the case of top-layer SLG transferred on Si<sub>3</sub>N<sub>4</sub>, FWHM(G) ~14 ± 1.2 cm<sup>-1</sup>, Pos(2D) ~2674.1 ± 0.9 cm<sup>-1</sup>, I(2D)/I(G) and A(2D)/A(G) are ~4.6 ± 0.5 and ~7.7 ± 0.7, respectively. The bottom-layer SLG, transferred and after hBN-capping, and top-layer SLG, are within the intrinsic SLG range in terms of doping (E<sub>F</sub> < 100 meV).<sup>98,99</sup> After Si<sub>3</sub>N<sub>4</sub> deposition, the bottom-layer E<sub>F</sub> increases to ~200 meV.<sup>98,99</sup> The linear fit to Pos(2D) as a function of Pos(G) in Fig.3b, gives ΔPos(2D)/ΔPos(G) ~ 0.78, ~0.66, ~1.41, ~1.22 for bottom-layer SLG transferred on SiO<sub>2</sub>, top-layer on Si<sub>3</sub>N<sub>4</sub>, bottom-layer after hBN capping, and bottom-layer after Si<sub>3</sub>N<sub>4</sub> deposition, respectively. This indicates the coexistence of strain and doping, modulated during the assembly steps. The presence (or coexistence) of biaxial strain cannot be ruled out. Considering the Grüneisen parameters ΔPos(G)/Δε ~ 23(60) cm<sup>-1</sup>/‰<sup>101-103</sup> and the unstrained, undoped Pos(G) ~ 1581.5 cm<sup>-1</sup><sup>92,104</sup> for intrinsic SLG (E<sub>F</sub> < 100 meV), we estimate a mean uniaxial(biaxial) strain ε ~ 0.07% (~0.03%) and ~0.03% (~0.01%), for SLG after transferring on SiO<sub>2</sub> (bottom-layer) and on Si<sub>3</sub>N<sub>4</sub> (top-layer), respectively. The bottom SLG after hBN capping has ε ~ 0.1% (~0.04%) while, after Si<sub>3</sub>N<sub>4</sub> deposition, considering doping,<sup>97</sup> ε ~ 0.25% (~0.1%).

To monitor the uniformity of the Raman response throughout the fabrication of the DSLG, we map 48 SLG SCs, 24 bottom-layer (b1-4 arrays) and 24 top-layer (t1-4 arrays), on 4 different portions of a 150 mm wafer. Fig.4 plots false-colour maps of I(D)/I(G), FWHM(2D), FWHM(G), A(2D)/A(G) for the 4 assembly stages. Each map is taken with 10 µm steps. At a given stage, the Raman data do not show significant variations between SLG belonging to the same portion of the wafer. The same applies between SLG from different parts.

This implies that the spread in points in Fig.4b-e is representative of the variation of the Raman peaks within individual SLG SCs, while over the scale of the entire wafer SLG SCs have uniform properties. Small (10-20  $\mu\text{m}$  wide) bilayer graphene (BLG) regions form at nucleation seeds during CVD (on 38/48 of the analysed crystals, see broad 2D peak central pixels in Fig. 4b<sup>92</sup>).

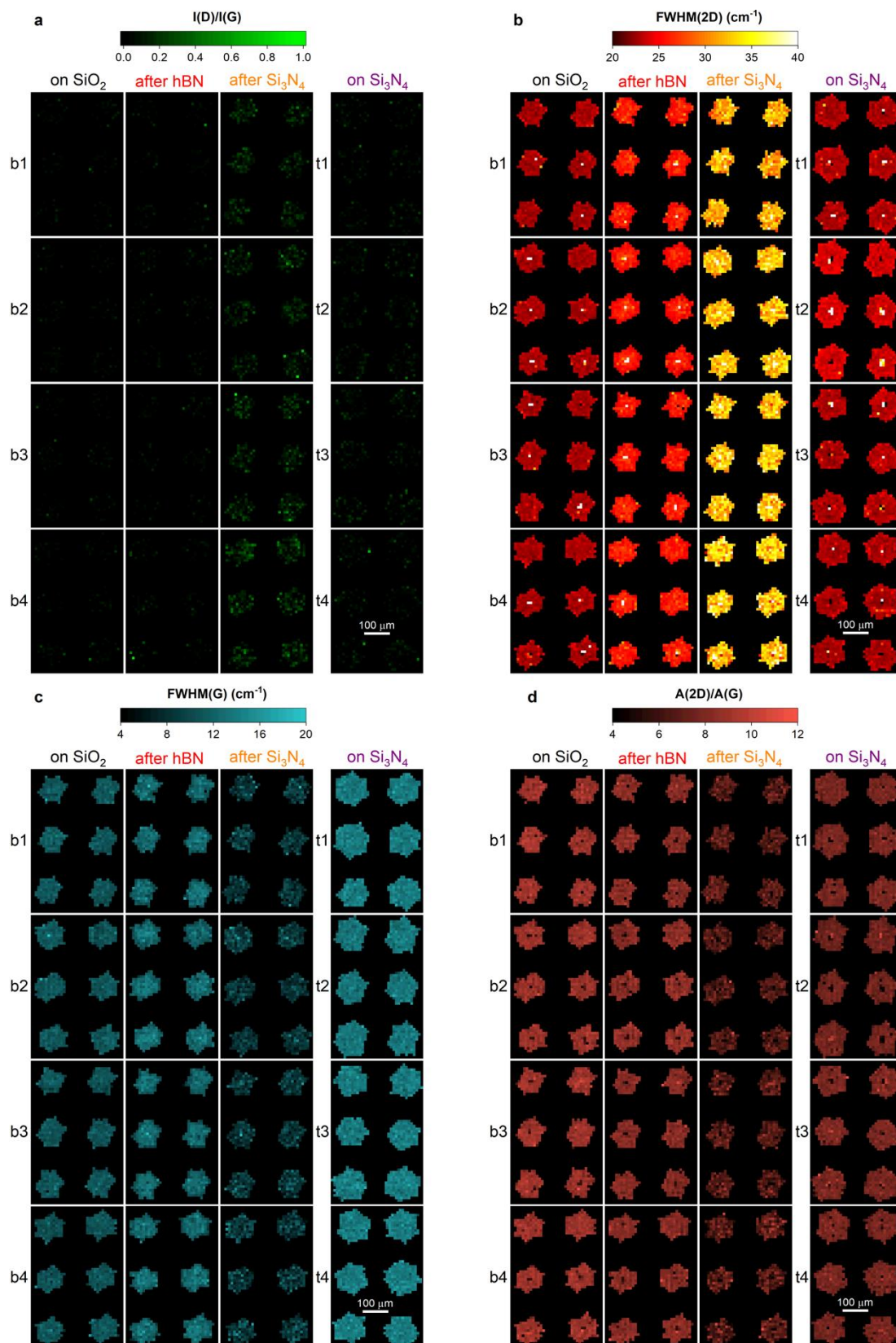


**Figure 4 . Wafer-scale Raman mapping at each fabrication step over different quadrants of the wafer. (a-d) Maps of I(D)/I(G), FWHM(2D), FWHM(G), A(2D)/A(G). Raman mapping is performed at each assembly stage over bottom (b1-4) and top SLG arrays (t1-4).**

I(D)/I(G), Fig.4a, is negligible throughout the fabrication, except for b1-4 after Si<sub>3</sub>N<sub>4</sub> deposition, where it is within 0.1 (0.25) for 59% (90%) of the crystals. FWHM(2D), Fig.4b, progressively increases upon fabrication on b1-4, while it is comparable for b1-4 and t1-4 after transfer on SiO<sub>2</sub> and Si<sub>3</sub>N<sub>4</sub>. FWHM(G) and A(2D)/A(G), Fig. 4c-d, are comparable for all SLG SCs, except for b1-4 after Si<sub>3</sub>N<sub>4</sub> deposition, where they decrease due to  $E_F > 100\text{meV}$ .

Thus, our wafer-scale Raman characterization reveals that the top-SLG in the DSLG is comparable to micro-mechanically exfoliated flakes in terms of doping,<sup>98</sup> strain<sup>107</sup> and strain fluctuations.<sup>108,109</sup> The transfer of hBN has marginal effect on the properties of the bottom-SLG, however it plays a key role in preserving the structural integrity of the crystals and avoid the formation of Raman-active defects during Si<sub>3</sub>N<sub>4</sub> deposition, thus avoiding  $\mu$  degradation. The Raman analysis shows an increase in doping, strain and strain fluctuations in the bottom SLG after the PECVD process, however, the PECVD process results in a homogeneous dielectric layer, crucial for reproducible operation of DSLG modulators.<sup>34</sup>

We then investigate the electrical transport properties of the transferred SLG-SCs using back-gated multi-terminal devices, at RT and exposed to air. This allows us to monitor two key performance parameters for SLG integration in a photonic circuit: contact resistance ( $R_c$ ) and  $\mu$ .

To quantify  $R_c$ , we use transfer-length method (TLM)<sup>110</sup> devices, as in Figs. 5a,b, defined by EBL, reactive-ion etching and thermal evaporation of metallic contacts. Ni/Au 7/60nm top contacts evaporated  $<10^{-5}$  mbar provide the highest performing configuration in terms of yield ( $>80\%$  of working devices) and  $R_c$  when compared to Cr, Ti and Ni and to other contact geometries, such as one-dimensional side contacts.<sup>111</sup> By measuring the two-terminal resistance over different channel lengths ( $l$ ) we extrapolate the residual resistance at  $l = 0$ , which corresponds to  $2 \times R_c$ ,<sup>110</sup> Fig.5c. This procedure can be repeated for different  $E_F$ , set by the back-gate voltage ( $V_G$ ), to obtain  $R_c$  as a function of  $E_F$ , as for Fig.5f, showing the statistical average over 56 devices and error bars as standard deviations.  $R_c$  remains  $<2500 \Omega \mu\text{m}$  in the neutrality region, and is as  $\sim 500 \Omega \mu\text{m}$  for  $E_F > 0.2$  eV, required in the operation of modulators at telecom wavelengths.<sup>2</sup> The SLG  $E_F$  must be set at energies larger than half of the photon energy in order to work at the edge of Pauli blocking.<sup>42,43,112</sup> At 1550 nm the photon energy is 0.8 eV, so that  $E_F$  must be set slightly above 0.4 eV.<sup>34</sup> These  $R_c$  are comparable to those previously reported for ultra-high  $\mu > 10^5 \text{ cm}^2 \text{ V}^{-1} \text{ s}^{-1}$  devices.<sup>111</sup> We get  $\mu$  from 56 TLM structures as well as 36 Hall bars, in Figs. 5d,f. The SLG resistivity,  $\rho$ , for the TLM devices is obtained from a linear fit of TLM channels (Fig. 5c) as a function of  $V_G$ . The Hall bar  $\rho$  is derived from 4-terminal measurements, and fitted as for Ref.<sup>113</sup> In Fig. 5g, dashed lines indicate the average  $\mu$  for both e and h, whereas the shaded areas represent the standard deviation. The average  $\mu$  from Hall bars ( $\sim 4750 \text{ cm}^2 \text{ V}^{-1} \text{ s}^{-1}$  for h and  $\sim 4600 \text{ cm}^2 \text{ V}^{-1} \text{ s}^{-1}$  for e) is higher than TLM ( $\sim 3600$  and

$\sim 3350 \text{ cm}^2 \text{ V}^{-1} \text{ s}^{-1}$ , respectively). This could be caused by two factors. 1) For each TLM,  $\rho$  is estimated from an average of 5 channels, with a total length of  $75 \text{ }\mu\text{m}$ , whereas the channel length in a Hall bar is  $8 \text{ }\mu\text{m}$ , comparable to that used in typical SLG transport measurements.<sup>113</sup> 2) Parasitic doping by the contacts has an effect in 2-terminal TLM measurements,<sup>114,115</sup> not present in 4-terminal Hall bar measurements.<sup>116</sup> Fig. 5h plots 3 representative traces of  $\rho$  as a function of  $V_G$ , from Hall bars with high ( $\sim 5900 \text{ cm}^2 \text{ V}^{-1} \text{ s}^{-1}$ ), low ( $\sim 3500 \text{ cm}^2 \text{ V}^{-1} \text{ s}^{-1}$ ) and average ( $\sim 4700 \text{ cm}^2 \text{ V}^{-1} \text{ s}^{-1}$ ) mobility.

EAMs are based on the modulation of the surface optical conductivity at optical frequencies induced by electric field effect.<sup>41,117</sup> SLG absorption is changed by moving  $E_F$  above the Pauli blocking condition.<sup>42,43,112</sup> This can be done by applying gating in a capacitor-like structure, with SLG on one or both capacitor plates.<sup>2</sup> In our DSLG geometry, a reciprocal self-gating is obtained with  $V_G$ , resulting in modulation of the surface carrier density, *i.e.* electro-absorption.<sup>34</sup> The main advantages of this approach are the larger electro-absorption effect, due to the presence of two SLG,  $\sim$ twice that of SLG,<sup>34</sup> and the possibility to use undoped WGs, enabling integration onto any already existing platform, such as SOI for Si photonics or  $\text{Si}_3\text{N}_4$  on Si.<sup>34</sup> Here we use a  $150 \text{ mm}$   $\text{Si}_3\text{N}_4$  photonic platform, with  $260 \text{ nm}$   $\text{Si}_3\text{N}_4$  on a  $15 \text{ }\mu\text{m}$  buried  $\text{SiO}_2$ . The  $1500 \text{ nm}$  wide WG is designed to support a transverse-electric field (quasi-TE) mode at  $1550 \text{ nm}$ .<sup>17</sup> The top cladding is thinned to  $\sim 40 \text{ nm}$  to maximize the evanescent coupling of the optical mode with the DSLG stack. The core of the modulators is the DSLG capacitor, comprising a SLG/hBN/ $\text{Si}_3\text{N}_4$ /SLG stack. The cross-section and a SEM image of a representative device is in Fig. 6a-b (see Methods for details). We prepare 30 SLG/hBN/ $\text{Si}_3\text{N}_4$ /SLG stacks on 30 WGs to fabricate 30 EAMs with different lengths (Fig. 6c-f). This allows us to benchmark the reproducibility of the fabrication process at wafer scale, through optoelectronic characterization of the devices.



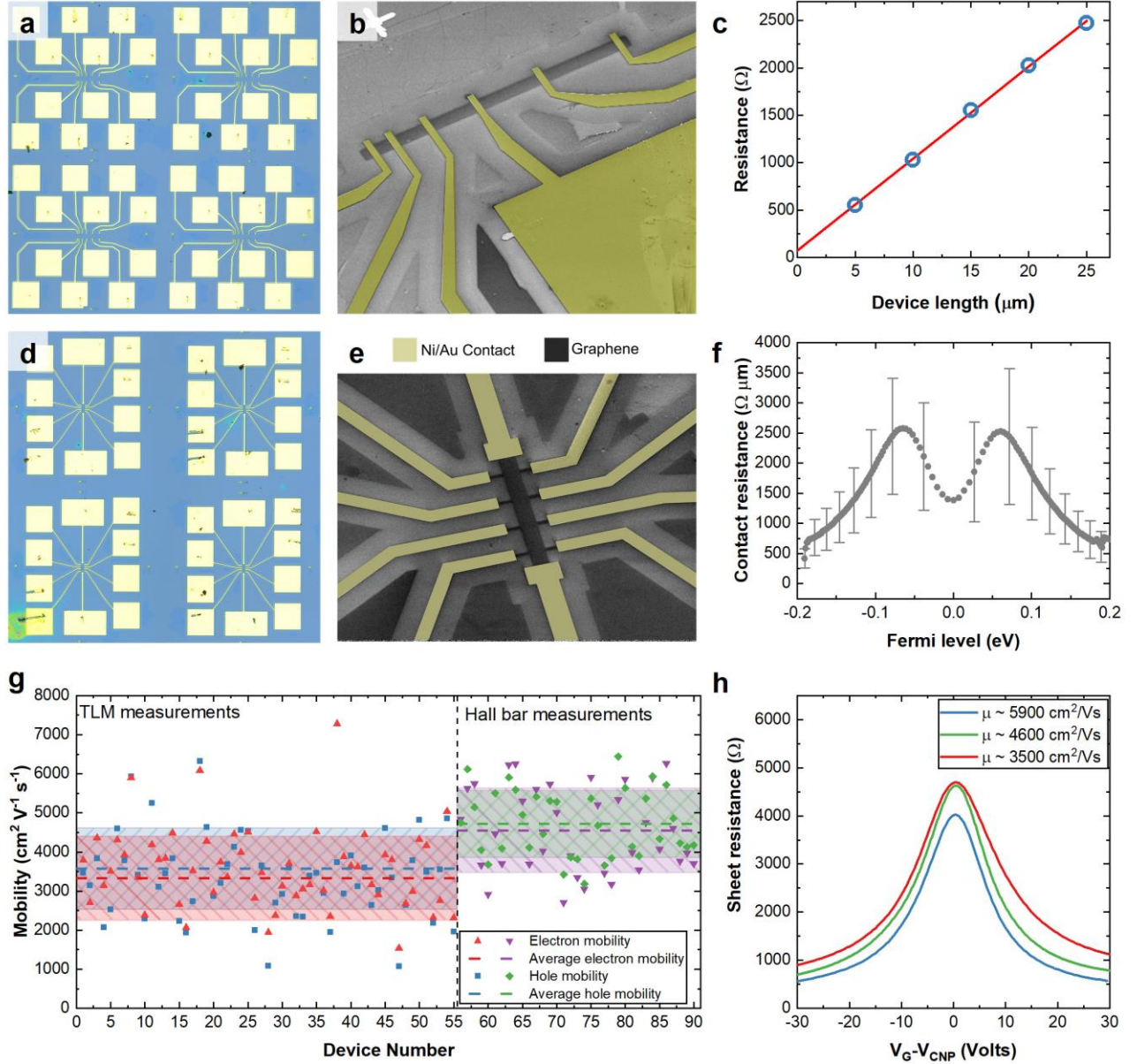


**Figure 5. Wafer-scale electrical characterisation. (a) Optical micrograph of TLM structures. (b) SEM image of representative TLM structure. (c) Estimation of  $R_C$  via linear fit of TLM measurements. (d) Optical micrograph of Hall bars. (e) SEM image of representative Hall bar. (f)  $R_C$  as a function of  $E_F$ . (g) Statistics of  $e$  and  $h$  mobility from TLM and Hall measurements. Dashed lines represent the average  $\mu$ . Shaded areas indicate the standard deviation. (h) Representative field effect curves for 3 Hall bars with  $\mu \sim 3500$ ,  $\sim 4600$  and  $\sim 5900 \text{ cm}^2 \text{ V}^{-1} \text{ s}^{-1}$ .**

We test key performance parameters: static (DC-biased) and dynamic (DC-biased + RF) modulation depth, electro-optical (EO) BW, and eye diagram opening. We characterize the EAMs in static and dynamic (*i.e.* driven by a time varying electrical signal) mode, and collect the data to perform a statistical study of performance, Fig.7. We first consider the transmission as a function of  $V_G$ . Modulation is obtained by tuning  $E_F$  of both SLG layers from complete optical absorption ( $E_F < 0.4$  eV at 1550 nm) towards transparency ( $E_F > 0.4$  eV).<sup>34</sup> The static characterization on wafer scale shows modulation efficiency  $\sim 0.25, 0.45, 0.75, 1 \text{ dB V}^{-1}$  for  $\sim 30, 60, 90, 120 \mu\text{m}$  EAMs, respectively,

Fig. 7a. We then characterize the EO BW, *i.e.* the BW of the conversion efficiency, defined as the ratio between the output and the input power,<sup>17</sup> from the electrical signal driving the modulator and the optical modulated signal at the output of the modulator.<sup>17</sup> This parameter determines the maximum operating speed, and is typically affected by  $R_C$ .<sup>118</sup> The EAM BW is mainly limited by its RC time constant,<sup>118</sup> *i.e.* the series resistance ( $R$ ) of the device multiplied by the DSLG capacitance,  $C$ , given by the series of gate dielectric capacitance and quantum capacitance of the two SLGs,<sup>119</sup> with  $R=R_C+R_S$  of the SLG section between DSLG capacitor and metal contacts. As  $C$  is proportional to the device length, while  $R$  is inversely proportional to it, we would expect a length independent 3 dB electro-optical BW.

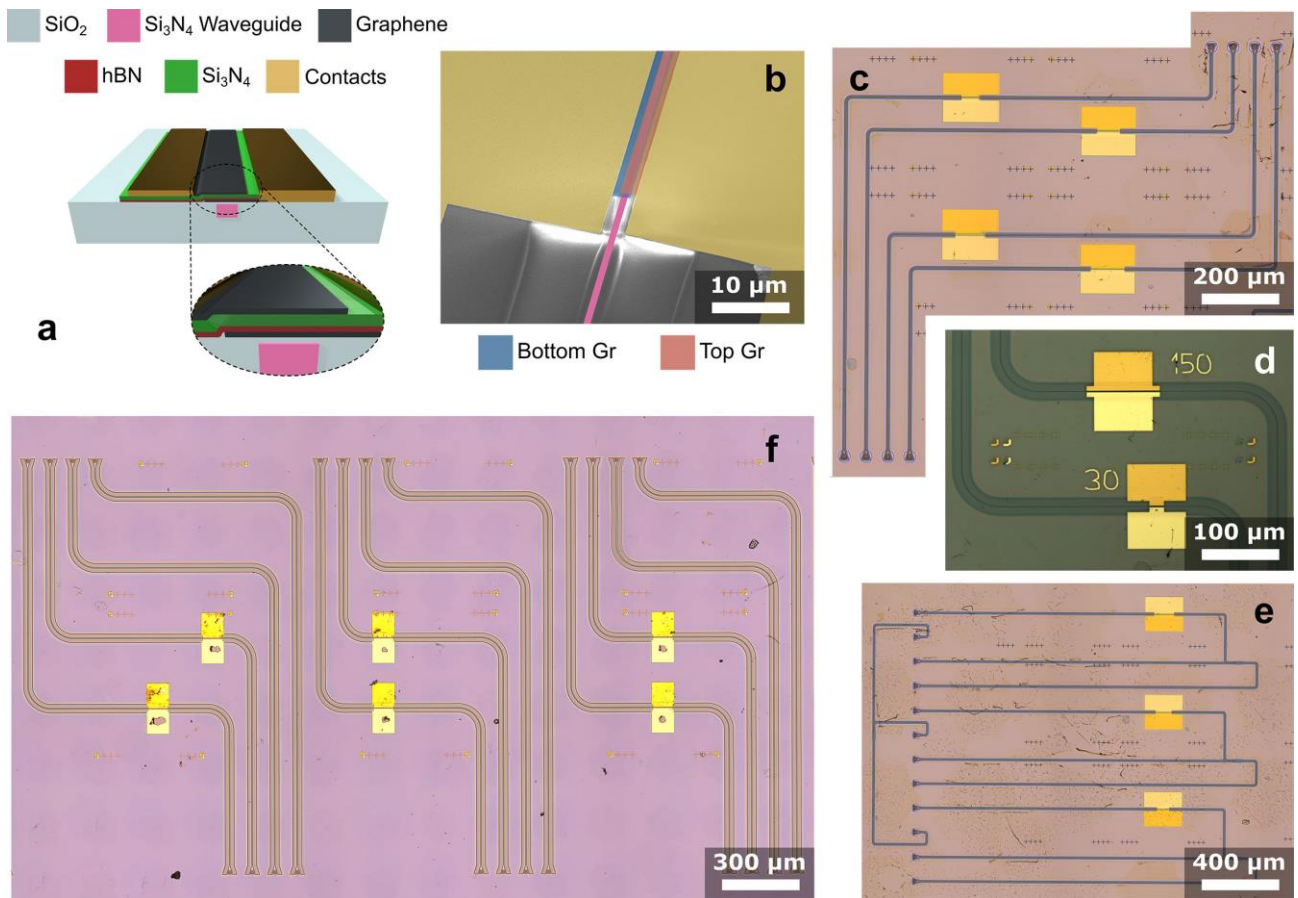


**Figure 6. DSLG modulators. (a) Cross-section of DSLG EAMs. The  $\text{Si}_3\text{N}_4$  WG core is 1500 nm wide and 260 nm thick, the buried oxide is 15  $\mu\text{m}$ , the distance of the metal electrodes from the WG edge is 700 nm (b) SEM image of DSLG EAM showing the overlap of the two SLG (blue and red) above the photonics WG (pink). (c-f) Optical micrographs of 4 chips with DSLG EAMs.**

However, Fig.7b shows that the BW changes with length, with longer devices having lower BW. We get ~11.5, 6.5, 7.4 GHz for 30, 60,120  $\mu\text{m}$ , respectively. The reason is that a further contribution to  $R$  comes from the output 50  $\Omega$  impedance of the Vector Network Analyzer (VNA) used to perform the measurements (see Methods). This is the main limiting resistive contribution because of our low  $R_C \sim 500 \Omega \mu\text{m}$  at  $E_F > 0.2 \text{ eV}$ .

We then test the DSLG EAMs using a non-return-to-zero (NRZ) electrical driving signal,<sup>58</sup> *i.e.* a digital two-level sequence, generated with a pattern generator (PG) (Anritzu MP1800A). This instrument allows us to obtain pseudo-random binary sequences (PRBS), *i.e.* deterministic binary sequences of bits with statistical behaviour similar to a pure random sequence,<sup>120</sup> with adjustable lengths (up to  $2^{31}-1$  bits). The signal is applied to the DSLG EAMs electrodes through a RF cable and a bias-tee. This generates a modulated optical signal, detected by a high-frequency (70 GHz) photodetector (Finisar XPDV3120) connected to a sampling digital oscilloscope (Infinium DCA 83484A, BW  $\sim 50$  GHz). By doing so, we can visualize on the oscilloscope the resulting eye diagram,<sup>121</sup> Fig. 7c. This gives the frequency dependent ER and 3 dB EO BW as a function of device length, and 10/15/20 Gbps data-rate.<sup>121</sup> The eye diagram measurement of the data stream along with ER and 3 dB EO BW demonstrate EAMs at 20 Gb s<sup>-1</sup> on wafer scale. Our wafer scale fabrication approach may also be used on different photonic platforms, *e.g.* SOI. The smaller WG cross section, 480 nm  $\times$  220 nm, would reduce modulator stack capacitance improving EAM speed.

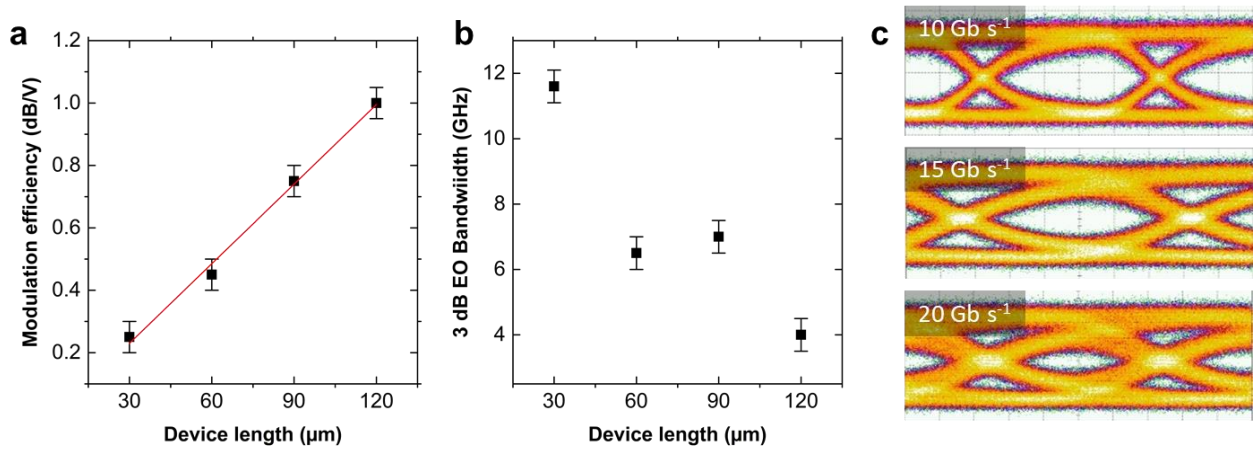


**Figure 7. DSLG EAM characterization. (a) Modulation efficiency as a function of device length. (b) 3 dB EO BW as a function of devices length (c) Eye diagrams at: 10, 15, 20 Gb s<sup>-1</sup>.**

The change from Si<sub>3</sub>N<sub>4</sub> to SOI, as reported in Ref.,<sup>47</sup> increases the EO BW to at least 30 GHz, and the data rate to 50 Gb s<sup>-1</sup> in a 100 μm EAM. Improving the SLG quality, in terms of  $\mu$  after Si<sub>3</sub>N<sub>4</sub> encapsulation, can increase performance in terms of insertion loss per unit length. Assuming a maximum absorption  $\sim 0.1$  dB  $\mu\text{m}^{-1}$  and  $< 0.001$  dB  $\mu\text{m}^{-1}$  in the transparency region for  $\mu > 3000$  cm<sup>2</sup> V<sup>-1</sup> s<sup>-1</sup> at 0.4 eV, the EAM length can be reduced to 50 μm with a maximum ER = 5 dB and a halved capacitance. By reducing the RC constant, we expect to approximately double its BW with respect to the 100 μm device, thus achieving  $\sim 60$  GHz. This optimization, combined with a SOI WG, could result in EAMs competitive with present microring based SOI modulators<sup>28,122</sup> and SiGe EAMs.<sup>29</sup> The extra value of SLG-based EAM is the broad operation spectrum, from O (1300 nm) to L-band ( $> 1625$  nm) and beyond, while SiGe modulators are restricted to the C band (1530 nm-1565 nm),<sup>123</sup> and the Si microring modulators are limited to the resonant wavelengths.<sup>124</sup>



## Conclusion

We presented the full process flow (from growth, to transfer, integration on WGs, and photonic devices fabrication) for SLG-based photonics on wafer-scale. Our approach yields high-quality highly-uniform SLG on wafer-scale, as indicated by statistical spectroscopic and electrical characterization. We used wafer scale hBN encapsulation to minimize damage during dielectric deposition. We applied this to realize double SLG electro-absorption modulators on the passive  $\text{Si}_3\text{N}_4$  platform. Our approach is easier and more reproducible in terms of yield and uniformity compared to the transfer of a continuous SLG film over the full wafer area, because the process is based on individual crystal matrices. SLG single crystals have higher mobility than polycrystalline films, with high-quality top contacts, with a reproducible contact resistance  $\sim 500 \Omega \mu\text{m}$ . Our approach can be used for other photonics building blocks, such as photodetectors or mixers.

## Methods

SLG crystal matrices are grown on  $25 \mu\text{m}$  Cu foils (Alfa Aesar #46365). Prior to SLG growth, each foil is electropolished in an electrolyte consisting of water, ethanol, phosphoric acid, isopropyl alcohol and urea, as for Ref.<sup>79</sup> The Cu foil is patterned using UV lithography. Cu is spin-coated with a Shipley S1813 positive photoresist, baked at  $110^\circ\text{C}$  for 1 min and exposed to UV light using a Cr mask containing the required seeding pattern (UV dose  $\sim 200 \text{ mJ cm}^{-2}$ ). 25 nm Cr is thermally evaporated (Sistec) at  $1 \times 10^{-5}$  mbar, followed by liftoff in acetone. The samples are then rinsed in isopropyl alcohol.

Growth is performed in an Aixtron BM Pro cold-wall reactor at 25 mbar and  $1060^\circ\text{C}$ . The samples are kept under Ar flow during the T ramp-up and are annealed for 10 min at the growth T. Growth is performed by flowing 0.5 sccm  $\text{CH}_4$ , 50 sccm  $\text{H}_2$  and 900 sccm Ar. Following the 20 min growth, the heating is switched off and the sample is cooled  $<120^\circ\text{C}$  under Ar flow.

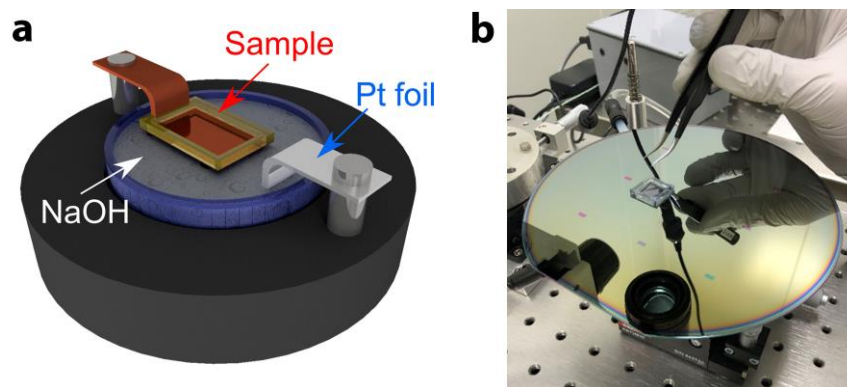


**Figure 8. (a) Schematic electrochemical delamination set-up. (b) SLG/PMMA membrane with a PDMS frame transferred on 150 mm  $\text{Si}_3\text{N}_4$  wafer.**

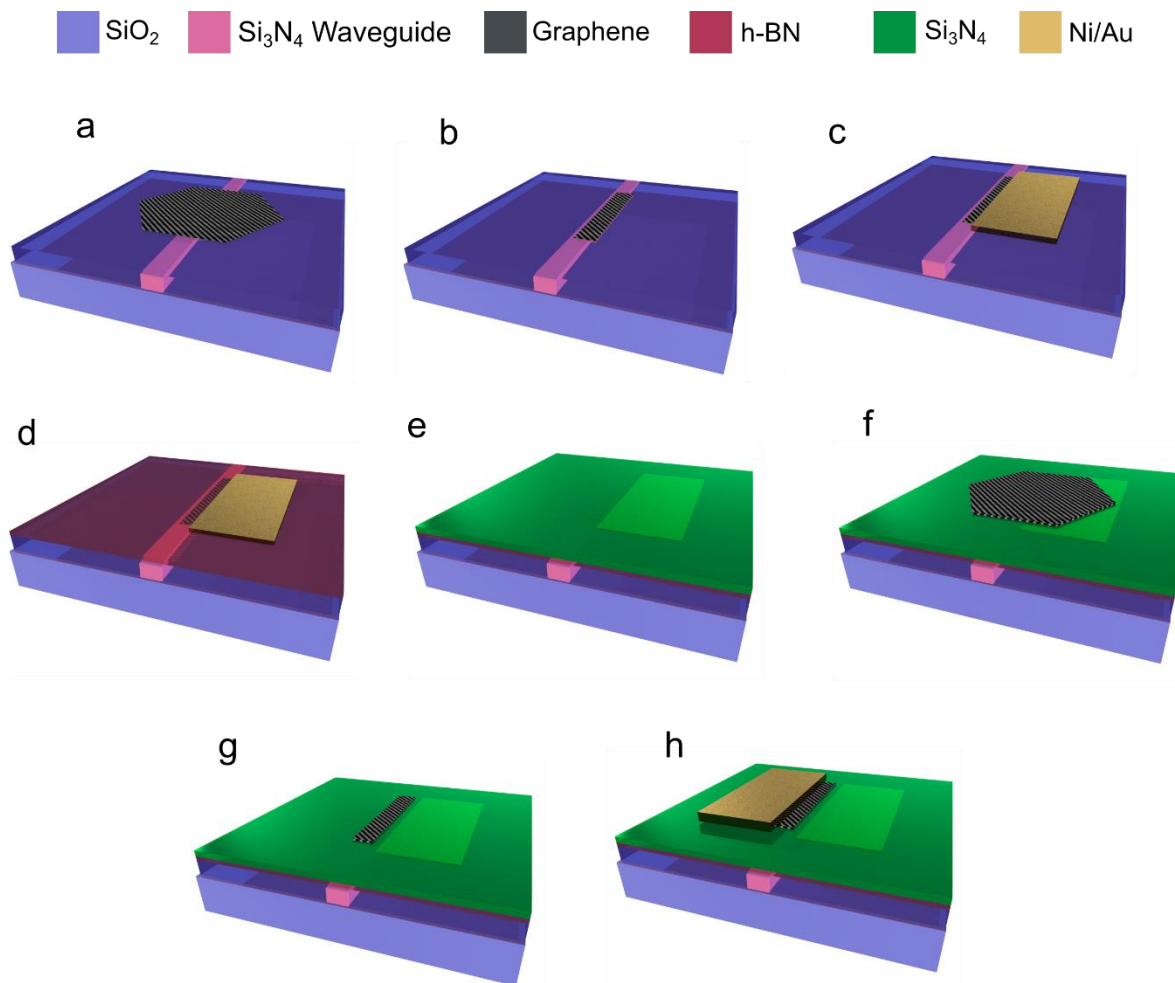


**Figure 9. Process flow for DSLG EAM fabrication. (a) SC SLG transferred on WG. (b) SLG is patterned using EBL and RIE. (c) Ni/Au contacts are deposited using evaporation and lift-off. (d) 1L-hBN is transferred on top. (e) Si<sub>3</sub>N<sub>4</sub> is deposited by PECVD. (f) Top layer SLG SC transfer. (g) Top SLG patterning. (h) Top contact deposition.**

SLG on Cu is then coated with a support polymer (100 nm PMMA 950K and 1.5  $\mu\text{m}$  PPC) and a PDMS frame is attached to the perimeter of the Cu foil. SLG electrochemical delamination is performed in 1M NaOH. Cu/SLG is used as the anode, and  $\sim 2.4$  V is applied with respect to a Pt counter electrode, Fig. 8a. The voltage is adjusted to maintain a current  $\sim 3$  mA, to avoid excessive formation of H<sub>2</sub> bubbles, which may cause damage to SLG. The freestanding polymer/SLG membrane is then removed from the electrolyte and rinsed 3 times in DI water, then dried in air.

The lamination of SLG on the target wafer is performed in a transfer tool, Fig. 8a. The target wafer is placed on a micrometric stage with 3-axis translational and azimuthal rotational movement, Fig. 8b. Alignment of the WGs to the SLG SC matrix is performed exploiting the SLG contrast on the polymer membrane in transmission mode, Fig. 1d. The optical system of the transfer tool consists of a 0.58x-7x microscope objective with coaxial illumination and a DSLR camera with a 2x adapter tube, giving a final magnification  $\sim 1.16\text{x}-14\text{x}$ . Following alignment, the wafer is heated to 100  $^{\circ}\text{C}$  using the inbuilt stage heater with a Proportional–Integral–Derivative (PID) controller, and the

membrane is brought into contact with the wafer to laminate the SLG. Heating the wafer reduces the adhesion of PDMS, and the frame can be then detached from the wafer, Fig. 7b. Depending on the geometry of the wafer, several cycles of the above procedure are performed to populate the wafer with SLG SCs. For a typical SLG SC matrix of 25×40 mm<sup>2</sup>, 16 cycles populate 90% of a 150 mm wafer. Finally, the wafer is placed in acetone to remove the support polymer, followed by a rinse in isopropyl alcohol.

The fabrication of the DSLG modulator stack is performed as follows. A matrix of SLG SCs is transferred on the target wafer, and aligned to the Si<sub>3</sub>N<sub>4</sub> WG, Fig. 9a. The bottom layer SLG is spin-coated with PMMA 950 A4 (Micro-chem), patterned using EBL and etched using RIE, Fig. 9b. Contacts to the bottom SLG are fabricated using EBL and thermal evaporation of 7 nm Ni and 60 nm Au, followed by lift-off in acetone, Fig. 9c. A 2×2.5 cm<sup>2</sup> polycrystalline 1L-hBN (Graphene Laboratories Inc) grown on Cu foil via CVD<sup>125</sup> is then electrochemically delaminated from Cu and transferred on the chips of the wafer *via* semi-dry transfer.<sup>76</sup> 17 nm Si<sub>3</sub>N<sub>4</sub> is deposited using PECVD at 350 °C, Fig. 9e. The top layer of the modulator is fabricated following the same protocol of transfer (Fig. 9f), etching (Fig. 9g), and contacting (Fig. 9h).

## Acknowledgements

We acknowledge funding from the European Union Graphene Flagship, ERC grants Hetero2D, GSYNCOR, EPSRC grants EP/L016087/1, EP/K01711X/1, EP/K017144/1.

## References

- (1) Bonaccorso, F.; Sun, Z.; Hasan, T.; Ferrari, A. C. Graphene Photonics and Optoelectronics. *Nat. Photonics* **2010**, 4, 611–622.
- (2) Romagnoli, M.; Sorianello, V.; Midrio, M.; Koppens, F. H. L.; Huyghebaert, C.; Neumaier, D.; Galli, P.; Templ, W.; D’Errico, A.; Ferrari, A. C. Graphene-Based Integrated Photonics for next-Generation Datacom and Telecom. *Nat. Rev. Mater.* **2018**, 3, 392–414.
- (3) Koppens, F. H. L.; Mueller, T.; Avouris, P.; Ferrari, A. C.; Vitiello, M. S.; Polini, M. Photodetectors Based on Graphene, Other Two-Dimensional Materials and Hybrid Systems. *Nat. Nanotechnol.* **2014**, 9, 780–793.
- (4) Ferrari, A. C.; Bonaccorso, F.; Fal’ko, V.; Novoselov, K. S.; Roche, S.; Bøggild, P.; Borini, S.; Koppens, F. H. L.; Palermo, V.; Pugno, N.; Garrido, J. A.; Sordan, R.; Bianco, A.; Ballerini, L.; Prato, M.; Lidorikis, E.; Kivioja, J.; Marinelli, C.; Ryhänen, T.; et al. Science and Technology Roadmap for Graphene, Related Two-Dimensional Crystals, and Hybrid Systems. *Nanoscale* **2015**, 7, 4598–4810.
- (5) Romagnoli, M. Graphene Photonics for Optical Communications. In *Optical Fiber Communication Conference (OFC) 2019*; OSA: Washington, D.C., 2019; p M3D.3.
- (6) Romagnoli, M. Graphene Photonics for Optical Communications. In *Broadband Access*



*Communication Technologies XIII*; Dingel, B. B., Tsukamoto, K., Mikroulis, S., Eds.; SPIE, 2019; p 1.

- (7) Cisco. Cisco Annual Internet Report (2018–2023). <https://www.cisco.com/c/en/us/solutions/collateral/executive-perspectives/annual-internet-report/white-paper-c11-741490.pdf> (accessed 2020-03-09).
- (8) Evans, D. The Internet of Things How the Next Evolution of the Internet Is Changing Everything. [https://www.cisco.com/c/dam/en\\_us/about/ac79/docs/innov/IoT\\_IBSG\\_0411FINAL.pdf](https://www.cisco.com/c/dam/en_us/about/ac79/docs/innov/IoT_IBSG_0411FINAL.pdf) (accessed 2011-04).
- (9) International Telecommunication Union. Definitions of World Telecommunication / Ict Indicators. [https://www.itu.int/ITU-D/ict/material/TelecomICT\\_Indicators\\_Definition\\_March2010\\_for\\_web.pdf](https://www.itu.int/ITU-D/ict/material/TelecomICT_Indicators_Definition_March2010_for_web.pdf) (accessed 2010-03).
- (10) Next Generation Mobile Networks Alliance. Next generation mobile 5G white paper. [https://www.ngmn.org/wp-content/uploads/NGMN\\_5G\\_White\\_Paper\\_V1\\_0.pdf](https://www.ngmn.org/wp-content/uploads/NGMN_5G_White_Paper_V1_0.pdf) (accessed 2015-02-17).
- (11) *Ericsson Mobility Report*. Available at: <https://www.ericsson.com/49da93/assets/local/mobility-report/documents/2020/june2020-ericsson-mobility-report.pdf> (accessed 2020-03).
- (12) How the Internet Can Cope With the Explosion of Demand for “Right Now” Data During the Coronavirus Outbreak <https://spectrum.ieee.org/tech-talk/telecom/internet/everyone-staying-home-because-of-covid19-is-targeting-the-internets-biggest-weak-spot> (accessed 2020-03-23).
- (13) 2020 Ethernet Roadmap <https://ethernetalliance.org/technology/2020-roadmap/> (accessed 2020-02-14).
- (14) Doerr, C. R. Silicon Photonic Integration in Telecommunications. *Front. Phys.* **2015**, 3.
- (15) Marchetti, R.; Lacava, C.; Carroll, L.; Gradkowski, K.; Minzioni, P. Coupling Strategies for Silicon Photonics Integrated Chips. *Photonics Res.* **2019**, 7, 201.
- (16) Selvaraja, S. K.; De Heyn, P.; Winroth, G.; Ong, P.; Lepage, G.; Cailler, C.; Rigny, A.; Bourdelle, K. K.; Bogaerts, W.; Van Thourhout, D.; Van Campenhout, J.; Absil, P. Highly Uniform and Low-Loss Passive Silicon Photonics Devices Using a 300mm CMOS Platform. In *Optical Fiber Communication Conference*; OSA: Washington, D.C., 2014; p Th2A.33.
- (17) Yariv, A.; Yariv, P. E. E. A.; Yeh, P. *Photonics: Optical Electronics in Modern Communications*; Oxford series in electrical and computer engineering; Oxford University Press, 2007.
- (18) PSM4MSAGroup. 100G PSM4 MSA Specification. <http://psm4.org/100G-PSM4-Specification-2.0.pdf> (accessed 2014-09-15).
- (19) Petrilla, J.; Cole, C.; King, J.; Lewis, D.; Hiramoto, K.; Tsumura, E. 100G CWDM4 MSA

Specifications. [http://www.cwdm4-msa.org/files/CWDM4\\_MSA\\_Technical\\_Spec\\_1p0.pdf](http://www.cwdm4-msa.org/files/CWDM4_MSA_Technical_Spec_1p0.pdf) (accessed 2014-08-27).

- (20) Miller, D. Device Requirements for Optical Interconnects to Silicon Chips. *Proc. IEEE* **2009**, 97, 1166–1185.
- (21) YOO, S. J. Ben. The Role of Photonics in Future Computing and Data Centers. *IEICE Trans. Commun.* **2014**, E97.B, 1272–1280.
- (22) Tekin, T.; Pleros, N.; Pitwon, R.; Hakansson, A. *Optical Interconnects for Data Centers*; Woodhead Publishing, 2016.
- (23) Colinge, J.-P. *Silicon-on-Insulator Technology: Materials to VLSI*; Springer US: Boston, MA, 1997.
- (24) Letal, G.; Prosyk, K.; Millett, R.; Macquistan, D.; Paquet, S.; Thibault-Maheu, O.; Gagné, J.; Fortin, P.; Dowlatshahi, R.; Rioux, B.; SpringThorpe, T.; Hisko, M.; Ma, R.; Woods, I. Low Loss InP C-Band IQ Modulator with 40GHz Bandwidth and 1.5V  $V_{\pi}$ . In *2015 Optical Fiber Communications Conference and Exhibition (OFC)*; 2015; pp 1–3.
- (25) Doerr, C.; Chen, L. Silicon Photonics in Optical Coherent Systems. *Proc. IEEE* **2018**, 106, 2291–2301.
- (26) Witzens, J. High-Speed Silicon Photonics Modulators. *Proc. IEEE* **2018**, 106, 2158–2182.
- (27) Valdar; Morfett. *Understanding Telecommunications Business*; Telecommunications; Institution of Engineering and Technology, 2015.
- (28) Tong, Y.; Hu, Z.; Wu, X.; Liu, S.; Chang, L.; Netherton, A.; Chan, C.-K.; Bowers, J. E.; Tsang, H. K. An Experimental Demonstration of 160-Gbit/s PAM-4 Using a Silicon Micro-Ring Modulator. *IEEE Photonics Technol. Lett.* **2020**, 32, 125–128.
- (29) Verbist, J.; Verplaetse, M.; Srinivasan, S. A.; Van Kerrebrouck, J.; De Heyn, P.; Absil, P.; De Keulenaer, T.; Pierco, R.; Vyncke, A.; Torfs, G.; Yin, X.; Roelkens, G.; Van Campenhout, J.; Bauwelinck, J. Real-Time 100 Gb/s NRZ and EDB Transmission With a GeSi Electroabsorption Modulator for Short-Reach Optical Interconnects. *J. Light. Technol.* **2018**, 36, 90–96.
- (30) Wang, B.; Huang, Q.; Chen, K.; Zhang, J.; Kurczveil, G.; Liang, D.; Palermo, S.; Tan, M. R. T.; Beausoleil, R. G.; He, S. MODULATION ON SILICON FOR DATACOM: PAST, PRESENT, AND FUTURE (INVITED REVIEW). *Prog. Electromagn. Res.* **2019**, 166, 119–145.
- (31) Smit, M.; Williams, K.; van der Tol, J. Past, Present, and Future of InP-Based Photonic Integration. *APL Photonics* **2019**, 4, 050901.
- (32) Yole Developpement. Silicon Photonics and Photonic Integrated Circuits 2019 by Yole Developpement. [https://www.slideshare.net/Yole\\_Developpement/silicon-photonics-and-photonic-](https://www.slideshare.net/Yole_Developpement/silicon-photonics-and-photonic-)

[integrated-circuits-2019-by-yole-dveloppement](#) (accessed 2019-04-25).

- (33) Comparison between InP and Silicon Photonics. <https://www.phiconference.com/market/comparison-between-inp-and-silicon-photonics/> (accessed 2015-06-17).
- (34) Sorianello, V.; Midrio, M.; Romagnoli, M. Design Optimization of Single and Double Layer Graphene Phase Modulators in SOI. *Opt. Express* **2015**, *23*, 6478.
- (35) Banszerus, L.; Schmitz, M.; Engels, S.; Dauber, J.; Oellers, M.; Haupt, F.; Watanabe, K.; Taniguchi, T.; Beschoten, B.; Stampfer, C. Ultrahigh-Mobility Graphene Devices from Chemical Vapor Deposition on Reusable Copper. *Sci. Adv.* **2015**, *1*, e1500222.
- (36) Purdie, D. G.; Pugno, N. M.; Taniguchi, T.; Watanabe, K.; Ferrari, A. C.; Lombardo, A. Cleaning Interfaces in Layered Materials Heterostructures. *Nat. Commun.* **2018**, *9*, 5387.
- (37) De Fazio, D.; Purdie, D. G.; Ott, A. K.; Braeuninger-Weimer, P.; Khodkov, T.; Goossens, S.; Taniguchi, T.; Watanabe, K.; Livreri, P.; Koppens, F. H. L.; Hofmann, S.; Goykhman, I.; Ferrari, A. C.; Lombardo, A. High-Mobility, Wet-Transferred Graphene Grown by Chemical Vapor Deposition. *ACS Nano* **2019**, *13*, 8926–8935.
- (38) Pezzini, S.; Mišeikis, V.; Pace, S.; Rossella, F.; Watanabe, K.; Taniguchi, T.; Coletti, C. High-Quality Electrical Transport Using Scalable CVD Graphene. *2D Mater.* **2020**, *7*, 041003.
- (39) Banszerus, L.; Sohler, T.; Epping, A.; Winkler, F.; Libisch, F.; Haupt, F.; Watanabe, K.; Taniguchi, T.; Müller-Caspary, K.; Marzari, N.; Mauri, F.; Beschoten, B.; Stampfer, C. Extraordinary High Room-Temperature Carrier Mobility in Graphene-WSe<sub>2</sub> Heterostructures. arXiv:1909.09523 <https://arxiv.org/abs/1909.09523> (accessed May 12, 2020)
- (40) Banszerus, L.; Schmitz, M.; Engels, S.; Goldsche, M.; Watanabe, K.; Taniguchi, T.; Beschoten, B.; Stampfer, C. Ballistic Transport Exceeding 28 Mm in CVD Grown Graphene. *Nano Lett.* **2016**, *16*, 1387–1391.
- (41) Novoselov, K. S.; Geim, A. K.; Morozov, S. V.; Jiang, D.; Zhang, Y.; Dubonos, S. V.; Grigorieva, I. V.; Firsov, A. A. Electric Field Effect in Atomically Thin Carbon Films. *Science*. **2004**, *306*, 666.
- (42) Wang, F.; Zhang, Y.; Tian, C.; Girit, C.; Zettl, A.; Crommie, M.; Shen, Y. R. Gate-Variable Optical Transitions in Graphene. *Science*. **2008**, *320*, 206–209.
- (43) Stauber, T.; Peres, N. M. R.; Geim, A. K. Optical Conductivity of Graphene in the Visible Region of the Spectrum. *Phys. Rev. B* **2008**, *78*, 085432.
- (44) Li, H.; Anugrah, Y.; Koester, S. J.; Li, M. Optical Absorption in Graphene Integrated on Silicon Waveguides. *Appl. Phys. Lett.* **2012**, *101*, 111110.
- (45) Liu, M.; Yin, X.; Zhang, X. Double-Layer Graphene Optical Modulator. *Nano Lett.* **2012**, *12*, 1482–

- (46) Liu, M.; Yin, X.; Ulin-Avila, E.; Geng, B.; Zentgraf, T.; Ju, L.; Wang, F.; Zhang, X. A Graphene-Based Broadband Optical Modulator. *Nature* **2011**, *474*, 64–67.
- (47) Giambra, M. A.; Sorianello, V.; Mišeikis, V.; Marconi, S.; Montanaro, A.; Galli, P.; Pezzini, S.; Coletti, C.; Romagnoli, M. High-Speed Double Layer Graphene Electro-Absorption Modulator on SOI Waveguide. *Opt. Express* **2019**, *27*, 20145–20155.
- (48) Midrio, M.; Galli, P.; Romagnoli, M.; Kimerling, L. C.; Michel, J. Graphene-Based Optical Phase Modulation of Waveguide Transverse Electric Modes. *Photonics Res.* **2014**, *2*, A34.
- (49) Sorianello, V.; Midrio, M.; Contestabile, G.; Asselberghs, I.; Van Campenhout, J.; Huyghebaert, C.; Goykhman, I.; Ott, A. K.; Ferrari, A. C.; Romagnoli, M. Graphene–Silicon Phase Modulators with Gigahertz Bandwidth. *Nat. Photonics* **2018**, *12*, 40–44.
- (50) Cassese, T.; Giambra, M. A.; Sorianello, V.; De Angelis, G.; Midrio, M.; Pantouvaki, M.; Van Campenhout, J.; Asselberghs, I.; Huyghebaert, C.; D’Errico, A.; Romagnoli, M. Capacitive Actuation and Switching of Add–Drop Graphene-Silicon Micro-Ring Filters. *Photonics Res.* **2017**, *5*, 762.
- (51) Song, J. C. W. W. C. W.; Rudner, M. S. S.; Marcus, C. M. M.; Levitov, L. S. S. Hot Carrier Transport and Photocurrent Response in Graphene. *Nano Lett.* **2011**, *11*, 4688–4692.
- (52) Muench, J. E.; Ruocco, A.; Giambra, M. A.; Mišeikis, V.; Zhang, D.; Wang, J.; Watson, H. F. Y.; Park, G. C.; Akhavan, S.; Sorianello, V.; Midrio, M.; Tomadin, A.; Coletti, C.; Romagnoli, M.; Ferrari, A. C.; Goykhman, I. Waveguide-Integrated, Plasmonic Enhanced Graphene Photodetectors. *Nano Lett.* **2019**, *19*, 7632–7644.
- (53) Shiue, R.-J.; Gao, Y.; Wang, Y.; Peng, C.; Robertson, A. D.; Efetov, D. K.; Assefa, S.; Koppens, F. H. L.; Hone, J.; Englund, D. High-Responsivity Graphene–Boron Nitride Photodetector and Autocorrelator in a Silicon Photonic Integrated Circuit. *Nano Lett.* **2015**, *15*, 7288–7293.
- (54) Mišeikis, V.; Marconi, S.; Giambra, M. A.; Montanaro, A.; Martini, L.; Fabbri, F.; Pezzini, S.; Piccinini, G.; Forti, S.; Terrés, B.; Goykhman, I.; Hamidouche, L.; Legagneux, P.; Sorianello, V.; Ferrari, A. C.; Koppens, F. H. L.; Romagnoli, M.; Coletti, C. Ultrafast, Zero-Bias, Graphene Photodetectors with Polymeric Gate Dielectric on Passive Photonic Waveguides. *ACS Nano* **2020**, *14*, 11190–11204.
- (55) Marconi, S.; Giambra, M. A.; Montanaro, A.; Mišeikis, V.; Soresi, S.; Tirelli, S.; Galli, P.; Buchali, F.; Templ, W.; Coletti, C.; Sorianello, V.; Romagnoli, M. Photo Thermal Effect Graphene Detector Featuring 105 Gbit S-1 NRZ and 120 Gbit s-1 PAM4 Direct Detection. arXiv:2006.01481 <https://arxiv.org/abs/2006.01481> (accessed 2020-06-02).
- (56) Phare, C. T.; Daniel Lee, Y.-H.; Cardenas, J.; Lipson, M. Graphene Electro-Optic Modulator with 30 GHz Bandwidth. *Nat. Photonics* **2015**, *9*, 511–514.

- (57) Jalali, B.; Fathpour, S. Silicon Photonics. *J. Light. Technol.* **2006**, *24*, 4600–4615.
- (58) Fathpour, S. *Handbook of Optoelectronics*; Dakin, J. P., Brown, R. G. W., Eds.; CRC Press: Second edition. | Boca Raton : Taylor & Francis, CRC Press, 2017.
- (59) Agrawal, G. P. *Lightwave Technology: Components and Devices*; John Wiley & Sons, 2004; Vol. 1.
- (60) Chrostowski, L.; Hochberg, M. *Silicon Photonics Design: From Devices to Systems*; Cambridge University Press, 2015.
- (61) Li, H. H. Refractive Index of Silicon and Germanium and Its Wavelength and Temperature Derivatives. *J. Phys. Chem. Ref. Data* **1980**, *9*, 561–658.
- (62) HORIZON 2020 - WORK PROGRAMME 2016– 2017  
[https://ec.europa.eu/research/participants/data/ref/h2020/other/wp/2016-2017/annexes/h2020-wp1617-annex-ga\\_en.pdf](https://ec.europa.eu/research/participants/data/ref/h2020/other/wp/2016-2017/annexes/h2020-wp1617-annex-ga_en.pdf) (accessed 2017-04-24).
- (63) Petrone, N.; Dean, C. R.; Meric, I.; van der Zande, A. M.; Huang, P. Y.; Wang, L.; Muller, D.; Shepard, K. L.; Hone, J. Chemical Vapor Deposition-Derived Graphene with Electrical Performance of Exfoliated Graphene. *Nano Lett.* **2012**, *12*, 2751.
- (64) Chen, X.; Wu, B.; Liu, Y. Direct Preparation of High Quality Graphene on Dielectric Substrates. *Chem. Soc. Rev.* **2016**, *45*, 2057–2074.
- (65) Mishra, N.; Forti, S.; Fabbri, F.; Martini, L.; McAleese, C.; Conran, B. R. R.; Whelan, P. R. R.; Shivayogimath, A.; Jessen, B. S. S.; Buß, L.; Falta, J.; Aliaj, I.; Roddaro, S.; Flege, J. I. I.; Bøggild, P.; Teo, K. B. K. B. K.; Coletti, C. Wafer-Scale Synthesis of Graphene on Sapphire: Toward Fab-Compatible Graphene. *Small* **2019**, *15*, 1904906.
- (66) Lee, J.-H.; Lee, E. K.; Joo, W.-J.; Jang, Y.; Kim, B.-S.; Lim, J. Y.; Choi, S.-H.; Ahn, S. J.; Ahn, J. R.; Park, M.-H.; Yang, C.-W.; Choi, B. L.; Hwang, S.-W.; Whang, D. Wafer-Scale Growth of Single-Crystal Monolayer Graphene on Reusable Hydrogen-Terminated Germanium. *Science*. **2014**, *344*, 286–289.
- (67) Lukosius, M.; Dabrowski, J.; Kitzmann, J.; Fursenko, O.; Akhtar, F.; Lisker, M.; Lippert, G.; Schulze, S.; Yamamoto, Y.; Schubert, M. A.; Krause, H. M.; Wolff, A.; Mai, A.; Schroeder, T.; Lupina, G. Metal-Free CVD Graphene Synthesis on 200 Mm Ge/Si(001) Substrates. *ACS Appl. Mater. Interfaces* **2016**, *8*, 33786–33793.
- (68) Scaparro, A. M.; Miseikis, V.; Coletti, C.; Notargiacomo, A.; Pea, M.; De Seta, M.; Di Gaspare, L. Investigating the CVD Synthesis of Graphene on Ge(100): Toward Layer-by-Layer Growth. *ACS Appl. Mater. Interfaces* **2016**, *8*, 33083–33090.
- (69) Li, X.; Cai, W.; An, J.; Kim, S.; Nah, J.; Yang, D.; Piner, R.; Velamakanni, A.; Jung, I.; Tutuc, E.; Banerjee, S. K.; Colombo, L.; Ruoff, R. S. Large-Area Synthesis of High-Quality and Uniform

Graphene Films on Copper Foils. *Science*. **2009**, 324, 1312–1314.

- (70) Bonaccorso, F.; Lombardo, A.; Hasan, T.; Sun, Z.; Colombo, L.; Ferrari, A. C. Production and Processing of Graphene and 2d Crystals. *Mater. Today* **2012**, 15, 564–589.
- (71) Backes, C.; Abdelkader, A. M.; Alonso, C.; Andrieux-Ledier, A.; Arenal, R.; Azpeitia, J.; Balakrishnan, N.; Banszerus, L.; Barjon, J.; Bartali, R.; Bellani, S.; Berger, C.; Berger, R.; Ortega, M. M. B.; Bernard, C.; Beton, P. H.; Beyer, A.; Bianco, A.; Bøggild, P.; et al. Production and Processing of Graphene and Related Materials. *2D Mater.* **2020**, 7, 022001.
- (72) Reina, A.; Jia, X.; Ho, J.; Nezich, D.; Son, H.; Bulovic, V.; Dresselhaus, M. S.; Kong, J. Large Area, Few-Layer Graphene Films on Arbitrary Substrates by Chemical Vapor Deposition. *Nano Lett.* **2009**, 9, 30–35.
- (73) Wang, Y.; Zheng, Y.; Xu, X.; Dubuisson, E.; Bao, Q.; Lu, J.; Loh, K. P. Electrochemical Delamination of CVD-Grown Graphene Film: Toward the Recyclable Use of Copper Catalyst. *ACS Nano* **2011**, 5, 9927–9933.
- (74) Gao, L.; Ren, W.; Xu, H.; Jin, L.; Wang, Z.; Ma, T.; Ma, L.-P.; Zhang, Z.; Fu, Q.; Peng, L.-M.; Bao, X.; Cheng, H.-M. Repeated Growth and Bubbling Transfer of Graphene with Millimetre-Size Single-Crystal Grains Using Platinum. *Nat. Commun.* **2012**, 3, 699.
- (75) Wang, R.; Whelan, P. R.; Braeuninger-Weimer, P.; Tappertzhofen, S.; Alexander-Webber, J. A.; Van Veldhoven, Z. A.; Kidambi, P. R.; Jessen, B. S.; Booth, T.; Bøggild, P.; Hofmann, S. Catalyst Interface Engineering for Improved 2D Film Lift-Off and Transfer. *ACS Appl. Mater. Interfaces* **2016**, 8, 33072–33082.
- (76) Miseikis, V.; Bianco, F.; David, J.; Gemmi, M.; Pellegrini, V.; Romagnoli, M.; Coletti, C. Deterministic Patterned Growth of High-Mobility Large-Crystal Graphene: A Path towards Wafer Scale Integration. *2D Mater.* **2017**, 4, 021004.
- (77) Sonntag, J.; Li, J.; Plaud, A.; Loiseau, A.; Barjon, J.; Edgar, J. H.; Stampfer, C. Excellent Electronic Transport in Heterostructures of Graphene and Monoisotopic Boron-Nitride Grown at Atmospheric Pressure. *2D Mater.* **2020**, 7, 031009.
- (78) Shivayogimath, A.; Whelan, P. R.; Mackenzie, D. M. A.; Luo, B.; Huang, D.; Luo, D.; Wang, M.; Gammelgaard, L.; Shi, H.; Ruoff, R. S.; Bøggild, P.; Booth, T. J. Do-It-Yourself Transfer of Large-Area Graphene Using an Office Laminator and Water. *Chem. Mater.* **2019**, 31, 2328–2336.
- (79) Miseikis, V.; Convertino, D.; Mishra, N.; Gemmi, M.; Mashoff, T.; Heun, S.; Haghghian, N.; Bisio, F.; Canepa, M.; Piazza, V.; Coletti, C. Rapid CVD Growth of Millimetre-Sized Single Crystal Graphene Using a Cold-Wall Reactor. *2D Mater.* **2015**, 2, 014006.
- (80) Alexander, K.; George, J. P.; Verbist, J.; Neyts, K.; Kuyken, B.; Van Thourhout, D.; Beeckman, J. Nanophotonic Pockels Modulators on a Silicon Nitride Platform. *Nat. Commun.* **2018**, 9, 3444.



- (81) Zurrón, Ó.; Picón, A.; Plaja, L. Theory of High-Order Harmonic Generation for Gapless Graphene. *New J. Phys.* **2018**, *20*, 053033.
- (82) Mohsin, M.; Schall, D.; Otto, M.; Noculak, A.; Neumaier, D.; Kurz, H. Graphene Based Low Insertion Loss Electro-Absorption Modulator on SOI Waveguide. *Opt. Express* **2014**, *22*, 15292.
- (83) Hao, Y.; Bharathi, M. S.; Wang, L.; Liu, Y.; Chen, H.; Nie, S.; Wang, X.; Chou, H.; Tan, C.; Fallahzad, B.; Ramanarayan, H.; Magnuson, C. W.; Tutuc, E.; Yakobson, B. I.; McCarty, K. F.; Zhang, Y.-W.; Kim, P.; Hone, J.; Colombo, L.; et al. The Role of Surface Oxygen in the Growth of Large Single-Crystal Graphene on Copper. *Science*. **2013**, *342*, 720–723.
- (84) Kang, S. J.; Kim, B.; Kim, K. S.; Zhao, Y.; Chen, Z.; Lee, G. H.; Hone, J.; Kim, P.; Nuckolls, C. Inking Elastomeric Stamps with Micro-Patterned, Single Layer Graphene to Create High-Performance OFETs. *Adv. Mater.* **2011**, *23*, 3531–3535.
- (85) SYLGARD™ 184 Silicone Elastomer Kit Technical Data Sheet <https://www.dow.com/en-us/document-viewer.html?randomVar=577327118110380375&docPath=/content/dam/dcc/documents/en-us/productdatasheet/11/11-31/11-3184-sylgard-184-elastomer.pdf> (accessed 2019-05-18).
- (86) Polymer Properties Database <http://polymerdatabase.com/polymer physics/Polymer Tg C.html>.
- (87) Coletti, C.; Giambra, M. A.; Miseikis, V.; Romagnoli, M. Metodo per Trasferire Grafene e Materiali Bidimensionali Mediante Membrana Polimerica a Doppio Strato Autoportante. 102019000005030, 2019.
- (88) Gao, L.; Ni, G.-X.; Liu, Y.; Liu, B.; Castro Neto, A. H.; Loh, K. P. Face-to-Face Transfer of Wafer-Scale Graphene Films. *Nature* **2014**, *505*, 190–194.
- (89) Kim, M.; Shah, A.; Li, C.; Mustonen, P.; Susoma, J.; Manoocheri, F.; Riikonen, J.; Lipsanen, H. Direct Transfer of Wafer-Scale Graphene Films. *2D Mater.* **2017**, *4*, 035004.
- (90) Zhu, W.; Neumayer, D.; Perebeinos, V.; Avouris, P. Silicon Nitride Gate Dielectrics and Band Gap Engineering in Graphene Layers. *Nano Lett.* **2010**, *10*, 3572–3576.
- (91) Single layer h-BN (Boron Nitride) film grown on copper foil: 2" x 1" <https://graphene-supermarket.com/Single-layer-h-BN-Boron-Nitride-film-grown-in-copper-foil-2-x-1.html> (accessed 2020-06-15).
- (92) Ferrari, A. C.; Meyer, J. C.; Scardaci, V.; Casiraghi, C.; Lazzeri, M.; Mauri, F.; Piscanec, S.; Jiang, D.; Novoselov, K. S.; Roth, S.; Geim, A. K. Raman Spectrum of Graphene and Graphene Layers. *Phys. Rev. Lett.* **2006**, *97*, 187401.
- (93) Ferrari, A. C.; Basko, D. M. Raman Spectroscopy as a Versatile Tool for Studying the Properties of Graphene. *Nat. Nanotechnol.* **2013**, *8*, 235–246.

- (94) Cançado, L. G.; Jorio, A.; Ferreira, E. H. M.; Stavale, F.; Achete, C. A.; Capaz, R. B.; Moutinho, M. V. O.; Lombardo, A.; Kulmala, T. S.; Ferrari, A. C.; Cancado, L. G.; Jorio, A.; Ferreira, E. H. M.; Stavale, F.; Achete, C. A.; Capaz, R. B.; Moutinho, M. V. O.; Lombardo, A.; Kulmala, T. S.; et al. Quantifying Defects in Graphene Via Raman Spectroscopy at Different Excitation Energies. *Nano Lett.* **2011**, 11, 3190.
- (95) Ni, Z. H.; Ponomarenko, L. A.; Nair, R. R.; Yang, R.; Anissimova, S.; Grigorieva, I. V.; Schedin, F.; Blake, P.; Shen, Z. X.; Hill, E. H.; Novoselov, K. S.; Geim, A. K. On Resonant Scatterers As a Factor Limiting Carrier Mobility in Graphene. *Nano Lett.* **2010**, 10, 3868–3872.
- (96) Chen, J.-H.; Cullen, W. G.; Jang, C.; Fuhrer, M. S.; Williams, E. D. Defect Scattering in Graphene. *Phys. Rev. Lett.* **2009**, 102, 236805.
- (97) Casiraghi, C.; Pisana, S.; Novoselov, K. S.; Geim, A. K.; Ferrari, A. C. Raman Fingerprint of Charged Impurities in Graphene. *Appl. Phys. Lett.* **2007**, 91, 233108.
- (98) Das, A.; Pisana, S.; Chakraborty, B.; Piscanec, S.; Saha, S. K.; Waghmare, U. V.; Novoselov, K. S.; Krishnamurthy, H. R.; Geim, A. K.; Ferrari, A. C.; Sood, A. K. Monitoring Dopants by Raman Scattering in an Electrochemically Top-Gated Graphene Transistor. *Nat. Nanotechnol.* **2008**, 3, 210–215.
- (99) Basko, D. M.; Piscanec, S.; Ferrari, A. C. Electron-Electron Interactions and Doping Dependence of the Two-Phonon Raman Intensity in Graphene. *Phys. Rev. B* **2009**, 80, 165413.
- (100) Bruna, M.; Ott, A. K.; Ijäs, M.; Yoon, D.; Sassi, U.; Ferrari, A. C. Doping Dependence of the Raman Spectrum of Defected Graphene. *ACS Nano* **2014**, 8, 7432–7441.
- (101) Mohiuddin, T. M. G.; Lombardo, A.; Nair, R. R.; Bonetti, A.; Savini, G.; Jalil, R.; Bonini, N.; Basko, D. M.; Galiotis, C.; Marzari, N.; Novoselov, K. S.; Geim, A. K.; Ferrari, A. C. Uniaxial Strain in Graphene by Raman Spectroscopy: G Peak Splitting, Grüneisen Parameters, and Sample Orientation. *Phys. Rev. B* **2009**, 79, 205433.
- (102) Yoon, D.; Son, Y. W.; Cheong, H. Strain-Dependent Splitting of the Double-Resonance Raman Scattering Band in Graphene. *Phys. Rev. Lett.* **2011**, 106, 155502.
- (103) Zabel, J.; Nair, R. R.; Ott, A.; Georgiou, T.; Geim, A. K.; Novoselov, K. S.; Casiraghi, C. Raman Spectroscopy of Graphene and Bilayer under Biaxial Strain: Bubbles and Balloons. *Nano Lett.* **2012**, 12, 617–621.
- (104) Piscanec, S.; Lazzeri, M.; Mauri, F.; Ferrari, A. C.; Robertson, J. Kohn Anomalies and Electron-Phonon Interactions in Graphite. *Phys. Rev. Lett.* **2004**, 93, 1–4.
- (105) Pisana, S.; Lazzeri, M.; Casiraghi, C.; Novoselov, K. S.; Geim, A. K.; Ferrari, A. C.; Mauri, F. Breakdown of the Adiabatic Born–Oppenheimer Approximation in Graphene. *Nat. Mater.* **2007**, 6, 198–201.

- (106) Tran, T. T.; Bray, K.; Ford, M. J.; Toth, M.; Aharonovich, I. Quantum Emission from Hexagonal Boron Nitride Monolayers. *Nat. Nanotechnol.* **2016**, 11, 37–41.
- (107) Lee, J. E.; Ahn, G.; Shim, J.; Lee, Y. S.; Ryu, S. Optical Separation of Mechanical Strain from Charge Doping in Graphene. *Nat. Commun.* **2012**, 3, 1024.
- (108) Neumann, C.; Reichardt, S.; Venezuela, P.; Drögeler, M.; Banszerus, L.; Schmitz, M.; Watanabe, K.; Taniguchi, T.; Mauri, F.; Beschoten, B.; Rotkin, S. V.; Stampfer, C. Raman Spectroscopy as Probe of Nanometre-Scale Strain Variations in Graphene. *Nat. Commun.* **2015**, 6, 8429.
- (109) Couto, N. J. G.; Costanzo, D.; Engels, S.; Ki, D.-K.; Watanabe, K.; Taniguchi, T.; Stampfer, C.; Guinea, F.; Morpurgo, A. F. Random Strain Fluctuations as Dominant Disorder Source for High-Quality On-Substrate Graphene Devices. *Phys. Rev. X* **2014**, 4, 041019.
- (110) Berger, H. H. Models for Contacts to Planar Devices. *Solid. State. Electron.* **1972**, 15, 145–158.
- (111) Wang, L.; Meric, I.; Huang, P. Y.; Gao, Q.; Gao, Y.; Tran, H.; Taniguchi, T.; Watanabe, K.; Campos, L. M.; Muller, D. A.; Guo, J.; Kim, P.; Hone, J.; Shepard, K. L.; Dean, C. R. One-Dimensional Electrical Contact to a Two-Dimensional Material. *Science.* **2013**, 342, 614–617.
- (112) Falkovsky, L. A. Optical Properties of Graphene. *J. Phys. Conf. Ser.* **2008**, 129, 012004.
- (113) Kim, S.; Nah, J.; Jo, I.; Shahrjerdi, D.; Colombo, L.; Yao, Z.; Tutuc, E.; Banerjee, S. K. Realization of a High Mobility Dual-Gated Graphene Field-Effect Transistor with Al<sub>2</sub>O<sub>3</sub> Dielectric. *Appl. Phys. Lett.* **2009**, 94, 062107.
- (114) Huard, B.; Stander, N.; Sulpizio, J. A.; Goldhaber-Gordon, D. Evidence of the Role of Contacts on the Observed Electron-Hole Asymmetry in Graphene. *Phys. Rev. B* **2008**, 78, 121402.
- (115) Lee, E. J. .; Balasubramanian, K.; Weitz, R. T.; BurkHard, M.; Kern, K. Contact and Edge Effects in Graphene Devices. *Nat. Nanotechnol.* **2008**, 3, 486–490.
- (116) Valdes, L. Resistivity Measurements on Germanium for Transistors. *Proc. IRE* **1954**, 42, 420–427.
- (117) Hanson, G. W. Dyadic Green's Functions and Guided Surface Waves for a Surface Conductivity Model of Graphene. *J. Appl. Phys.* **2008**, 103, 064302.
- (118) Alexander, C. K. *Fundamentals of Electric Circuits*; McGraw-Hill, 2009.
- (119) Xia, J.; Chen, F.; Li, J.; Tao, N. Measurement of the Quantum Capacitance of Graphene. *Nat. Nanotechnol.* **2009**, 4, 505–509
- (120) Seimetz, M. *High-Order Modulation for Optical Fiber Transmission*; Springer Series in Optical Sciences; Springer Berlin Heidelberg, 2009.
- (121) Razavi, B. *Design of Integrated Circuits for Optical Communications*; John Wiley & Sons, 2012.

- (122) Pitris, S.; Moralis-Pegios, M.; Alexoudi, T.; Fotiadis, K.; Ban, Y.; Heyn, P. De; Campenhout, J. Van; Pleros, N. A 400 Gb/s O-Band WDM (8×50 Gb/s) Silicon Photonic Ring Modulator-Based Transceiver. In *2020 Optical Fiber Communications Conference and Exhibition (OFC)*; 2020; pp 1–3.
- (123) Chaisakul, P.; Vakarin, V.; Frigerio, J.; Chrastina, D.; Isella, G.; Vivien, L.; Marris-Morini, D. Recent Progress on Ge/SiGe Quantum Well Optical Modulators, Detectors, and Emitters for Optical Interconnects. *Photonics* **2019**, 6, 24.
- (124) Optical Microresonator Theory. In *Optical Microresonators*; Heebner, J., Grover, R., Ibrahim, T., Eds.; Springer New York: New York, NY, 2008; pp 71–103.
- (125) Kim, K. K.; Hsu, A.; Jia, X.; Kim, S. M.; Shi, Y.; Hofmann, M.; Nezich, D.; Rodriguez-Nieva, J. F.; Dresselhaus, M.; Palacios, T.; Kong, J. Synthesis of Monolayer Hexagonal Boron Nitride on Cu Foil Using Chemical Vapor Deposition. *Nano*